

RL-TR-96-65
In-House Report
May 1996



ANTI-JAMMING OPTICAL BEAM NULLER

Michael E. Turbyfill, 1Lt, USAF
Jeffrey M. Lutsko, 1 Lt, USAF

APPROVED FOR PUBLIC RELEASE; DISTRIBUTION UNLIMITED.

19960724 060

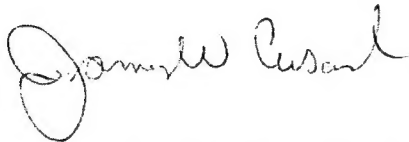
DTIC QUALITY INSPECTED 3

Rome Laboratory
Air Force Materiel Command
Rome, New York

This report has been reviewed by the Rome Laboratory Public Affairs Office (PA) and is releasable to the National Technical Information Service (NTIS). At NTIS it will be releasable to the general public, including foreign nations.

RL-TR-96-65 has been reviewed and is approved for publication.

APPROVED:



JAMES W. CUSACK, Chief
Photonics Division
Surveillance and Photonics Directorate

FOR THE COMMANDER:



GARY D. BARMORE, Maj, USAF
Deputy Director
Surveillance & Photonics Directorate

If your address has changed or if you wish to be removed from the Rome Laboratory mailing list, or if the addressee is no longer employed by your organization, please notify Rome Laboratory/OCPC, Rome, NY 13441. This will assist us in maintaining a current mailing list.

Do not return copies of this report unless contractual obligations or notices on a specific document require that it be returned.

REPORT DOCUMENTATION PAGE

Form Approved
OMB No. 0704-0188

Public reporting burden for this collection of information is estimated to average 1 hour per response, including the time for reviewing instructions, searching existing data sources, gathering and maintaining the data needed, and completing and reviewing the collection of information. Send comments regarding this burden estimate or any other aspect of this collection of information, including suggestions for reducing this burden, to Washington Headquarters Services, Directorate for Information Operations and Reports, 1215 Jefferson Davis Highway, Suite 1204, Arlington, VA 22202-4302, and to the Office of Management and Budget, Paperwork Reduction Project (0704-0188), Washington, DC 20503.

1. AGENCY USE ONLY (Leave Blank)		2. REPORT DATE May 1996	3. REPORT TYPE AND DATES COVERED In-House Oct 92 - Sep 95	
4. TITLE AND SUBTITLE ANTI-JAMMING OPTICAL BEAM NULLER			5. FUNDING NUMBERS PE - 62702F PR - 4600 TA - P1 WU - 14	
6. AUTHOR(S) Michael E. Turbyfill, 1Lt, USAF; Jeffrey M. Lutsko, 1Lt, USAF				
7. PERFORMING ORGANIZATION NAME(S) AND ADDRESS(ES) Rome Laboratory/OCPC 25 Electronic Pky Rome, NY 13441-4515			8. PERFORMING ORGANIZATION REPORT NUMBER RL-TR-96-65	
9. SPONSORING/MONITORING AGENCY NAME(S) AND ADDRESS(ES) Rome Laboratory/OCPC 25 Electronic Pky Rome, NY 13441-4515			10. SPONSORING/MONITORING AGENCY REPORT NUMBER	
11. SUPPLEMENTARY NOTES Rome Laboratory Project Engineer: Michael E. Turbyfill, 1Lt, USAF, 315-330-7588				
12a. DISTRIBUTION/AVAILABILITY STATEMENT Approved for public release, distribution unlimited.			12b. DISTRIBUTION CODE	
13. ABSTRACT (Maximum 200 words) The development of an Acousto-optic (AO) based anti-jamming optical beam nuller (AJOB), including laboratory and live radar tests, is presented. The purpose of the AJOB system is the cancellation of multipath jamming interference in advanced surveillance radars. AJOB is a multichannel adaptive optical system which performs cancellation of multiple wideband (10 MHz) interference sources in the presence of multipath. The live radar test consisted of using a downconverted 80 MHz received signal from the main and subarrays of a C-band radar to correlate jamming signals produced by stationary jammers. The correlation parameters fed a tapped delay line filter to form an estimate of the noise, which was subtracted from the main antenna signal. For the scenarios tested, the long integration time for the correlation data provided accurate estimates of the jammer delays, and therefore single-step convergence was achieved.				
14. SUBJECT TERMS least mean square algorithm, adaptive optical processing, acousto-optics, phased array radar, Bragg angle, correlator			15. NUMBER OF PAGES 60	
			16. PRICE CODE	
17. SECURITY CLASSIFICATION OF REPORT UNCLASSIFIED	18. SECURITY CLASSIFICATION OF THIS PAGE UNCLASSIFIED	19. SECURITY CLASSIFICATION OF ABSTRACT UNCLASSIFIED	20. LIMITATION OF ABSTRACT U/L	

Table of Contents

	Page
Acknowledgements	v
1 Introduction	1
2 Applications of Adaptive Processing to Jamming Cancellation	2
2.1 Radar Signal Processing Scenario	2
2.2 Applications of the LMS Algorithm	5
3 AJOB System Design Considerations	7
3.1 Overall Considerations	7
3.2 Time-Integrating Correlator	8
3.2.1 Mach-Zehnder Time-Integrating Correlator	10
3.2.2 In-Line Time-Integrating Correlator	13
3.2.3 Mach-Zehnder Experimental Setup	19
3.2.4 In-Line Time-Integrating Correlator Experimental Setup	20
3.3 Interface Techniques	22
3.3.1 Computer Software	23
3.4 Acousto-Optic Tapped Delay Line	24
3.4.1 Tapped Delay Line Experimental Setup	25
3.5 Single-Loop Electronic Canceller	27
4 Phased Array Radar Tests	28
4.1 Radar Facility Description	29
4.2 Test Setup	30
5 Data	33
5.1 Correlator Architecture Dynamic Range Considerations	33
5.2 Test Results for Software Based Signal Processing	38
5.3 Acousto-Optic Tapped Delay Line Test Results	40
5.4 Experimental Test Results	41
6 Summary and Conclusions	44
REFERENCES	46

List of Illustrations

Figure	Page
1 Radar signal processing scenario	3
2 AJOB system within radar system	4
3 AJOB system layout for two channels	8
4 Mach-Zehnder interferometric time-integrating correlator	11
5 Conceptual diagram of autocorrelation with Mach-Zehnder correlator	12
6 In-Line interferometric time-integrating correlator	13
7 The Dove prism	14
8 Paths of diffracted and undiffracted light from AO1 to AO2	16
9 Fringe spacing versus input frequency for various focal length lenses	19
10 Mach-Zehnder time-integrating correlator experimental layout	20
11 In-Line time-integrating correlator experimental layout	21
12 Computer controlled interface	23
13 AOSLM used to tap AOTDL	26
14 Electronic canceller configuration	27
15 Rome Laboratory ECCM antenna used in live tests	28
16 Remote jammer site	30
17 Azimuth antenna patterns showing jammer and target locations	32
18 Dynamic range test signal generation layout	34
19 Input signals for dynamic range testing	34
20 Dynamic range test for Mach-Zehnder correlator at 0 dB attenuation	35
21 Dynamic range test for Mach-Zehnder correlator at 20 dB attenuation	35
22 Dynamic range test for Mach-Zehnder correlator at 27 dB attenuation	36
23 Dynamic range test for in-line correlator at 0 dB attenuation	36
24 Dynamic range test for in-line correlator at 20 dB attenuation	37
25 Dynamic range test for in-line correlator at 29 dB attenuation	37
26 Raw detector output	39
27 Background non-uniformities subtracted	39
28 Normalized peak pixel location	40
29 Various AOTDL frequency responses	41
30 AOTDL frequency response for 25 MHz span	41
31 Phase I phased-array radar cancellation results	42
32 Phase II phased array radar cancellation results	44

List of Tables

Table	Page
1 Short and long term design requirements	7

Acknowledgements

The in-house AJOB team recognizes the important contributions of the Dynetics Inc. staff: Dr. Merv Budge, Dr. Bob Berinato, and Mr. Michael Zari. None of the radar testing would have been possible without the help of Mr. Mark Rudd. Special thanks to Captains Michael Ward, Chris Keefer, and Andy Andrews for initial work performed on the MADOP/AJOB systems.

1. Introduction

The Air Force is continually looking to optical signal processing for improvements to surveillance radars in an increasingly dense electronic warfare arena. Specifically, an efficient processing system which can adaptively cancel multisource multipath jamming noise will be an asset in the future. Because of practical limitations (e.g., speed, size, signal bandwidth, inability to perform parallel processing) existing digital electronic processors inadequately address the problem of cancelling wideband multipath interference. Digital sidelobe cancellers require a separate processing channel for every multipath interference source. Each processing channel must include a discretely tapped radio frequency (RF) delay line of length equal to or greater than the maximum multipath delay expected.

Optical signal processing offers attractive alternatives to digital signal processors. A single AO time-integrating correlator could replace digital equipment in computing the correlation of the wide bandwidth signals received by an antenna. Furthermore, an AO based RF delay line provides long delays and extremely fine tap resolutions. The merger of AO correlator and AO delay line circuits allows for massively parallel computations. The AO based adaptive processor described here represents a potential solution to the problem of multisource multipath jamming noise. Preliminary live radar tests indicate about 25 dB cancellation of continuous wave (CW) jammer noise and 15 dB cancellation of barrage jamming noise.

There have been many architectures designed and tested to implement antenna sidelobe interference cancellation. One such project, the Acousto-Optic Null Steering Processor (AONSP) funded by the Advanced Research Projects Agency in conjunction with Rome Laboratory, took place from May, 1991 through April, 1995 at the Lockheed Martin facilities in Syracuse, New York [1]. The AONSP utilizes a photorefractive crystal for the processor's temporal integrator. The University of Colorado at Boulder is

also using a photorefractive crystal in their investigation of three dimensional photorefractive signal processing in radar applications [2].

2. Applications of Adaptive Processing to Jamming Cancellation

2.1 Radar Signal Processing Scenario

Previous theoretical work, forming a solid foundation for this project, has been around for many years [3], [4], [5]. It is important, though, to review the applications of adaptive processing to jamming cancellation. The scenario considered is an antenna array with one directional main antenna and R omni-directional auxiliary antennas. Figure 1 depicts this scenario, with an array attempting to detect a target return, $s(t)$, in the presence of P broadband noise jammers, where $P \leq R$. In the case of Figure 1 there is only one jamming source, for simplicity. The main antenna receives $s(t)$ into the main receiving lobe and a mix of noise signals and multipath reflections of noise coupled into the sidelobes. Instead of simply receiving $s(t)$, the composite signal received by the main antenna is $d(t)$, which for the case of two jammers ($P = 2$) is

$$d(t) = s(t) + \sum_{m=1}^{M_{01}} A_{01m} \cdot n_1(t - \tau_{01m}) + \sum_{m=1}^{M_{02}} A_{02m} \cdot n_2(t - \tau_{02m}), \quad (1)$$

where $n_p(t)$, for all $1 \leq p \leq P$, is the noise signal from the p th jammer source. M_{0p} represents the total number of multipath reflections from the p th jammer received by the main antenna. The A_{0pm} , for all $1 \leq m \leq M_{0p}$, represent the received gain of the m th multipath reflection from the p th jamming source into the main antenna, and are a function of the amplitude of the reflection and the sidelobe gain. The multipath delays, τ_{0pm} , represent the time delay of the m th multipath reflection from the p th jamming source in traveling to the main antenna.

In addition to this main channel signal, each of the R auxiliary antennas receives a composite noise signal, $N_r(t)$, for all $1 \leq r \leq R$. Note that the $r = 0$ case represents the main antenna. The composite noise signal for the r th auxiliary can be expressed as

$$N_r(t) = \sum_{p=1}^P \sum_{m=1}^{M_{rp}} A_{rpm} \cdot n_p(t - \tau_{rpm}), \quad (2)$$

in which M_{rp} represents the total number of multipath reflections from the p th jammer into the r th antenna element. Also, the A_{rpm} represent the received gain of the m th multipath reflection from the p th jamming source into the r th antenna element, and are a function of the multipath amplitude and antenna gain. The multipath delays, τ_{rpm} , are defined similarly [6].

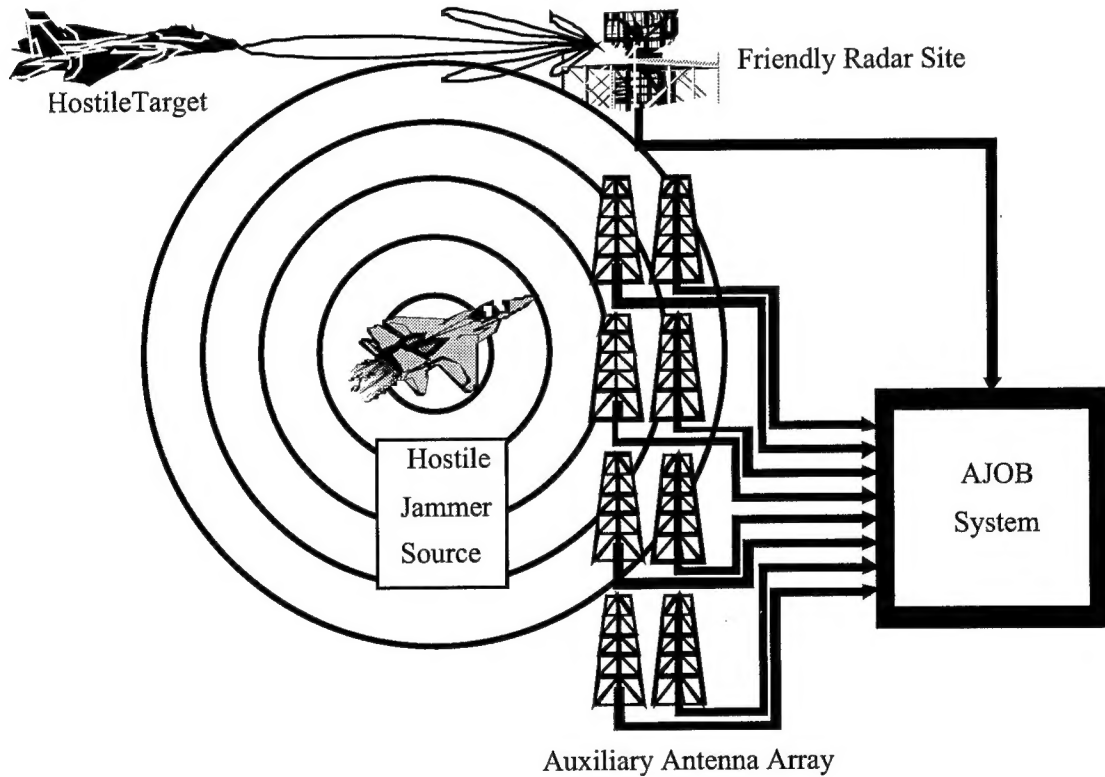


Figure 1. Radar signal processing scenario. *Surveillance radars in the presence of interference sources can suffer greatly from reduced signal-to-noise ratios, and may be rendered useless under certain hostile conditions without the use of jammer nulling.*

It is assumed that the interference noise is on the order of, or much larger than the target return, $s(t)$, resulting in a negative signal-to-jammer (S/J) ratio in the main antenna. The auxiliary antennas receive interference noise, but the target return entering these antennas is negligible because of the low main channel S/J assumption. The output from the main antenna and each of the auxiliary antennas is mixed down to a system intermediate frequency (IF), as shown in Figure 2. Digital post processing systems require a low noise signal, $s(t)$, in order to accurately detect and identify the target, however, the jammer noise term present in $d(t)$ masks the target return.

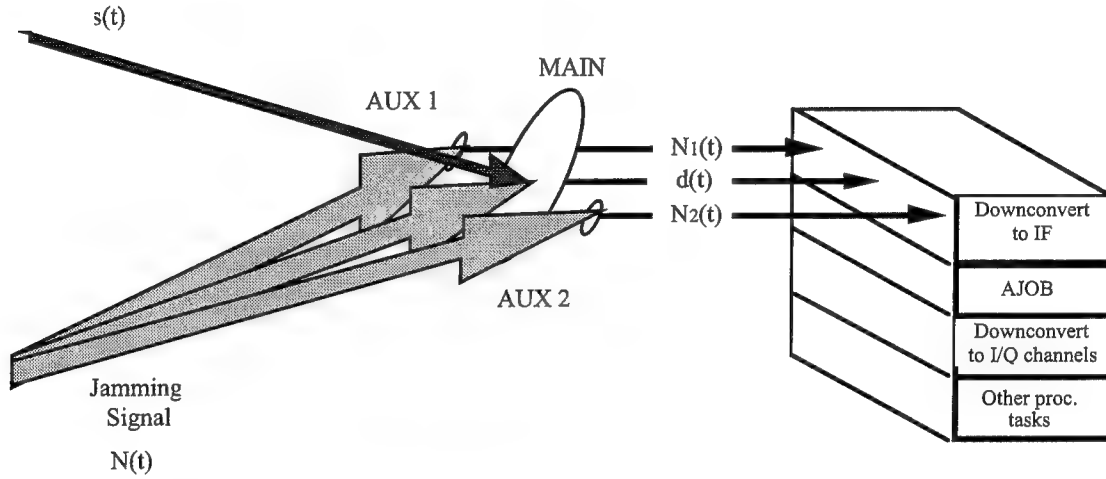


Figure 2. AJOB system within radar system.

Figure 2 shows that the AJOB system receives signal inputs at the system IF from the main antenna and each of the auxiliary antennas (two for this figure). After performing its adaptive cancellation task, the AJOB system suppresses the noise and extracts the target signal $s(t)$, to be used in other signal processing tasks. Assuming, as stated before, that the target return, $s(t)$, is of negligible amplitude relative to the noise amplitudes at each of the auxiliary antennas, this problem calls for an application of an adaptive algorithm such as least mean squares (LMS). The LMS algorithm makes use of the auxiliary antenna inputs in forming an estimate of the noise in $d(t)$, as will be explained in the next section.

2.2 Application of the LMS Algorithm

Widrow and Stearns described applications of the LMS algorithm to such problems as extracting a fetal heartbeat from the mother's heartbeat, or cancelling surface acoustic noise from a geologic sensor [7]. The approach taken under the AJOB system falls into this same category of adaptive noise cancellation. When fed a main signal, $d(t)$, consisting of a target return and noise, and a reference signal, $N_r(t)$, containing correlated and possibly delayed versions of the noise, the LMS algorithm uses a weight vector, $w_r(\tau)$, to tap a delay line containing the r th reference signal. The output from the tapped delay line forms the noise signal estimate, $y(t)$. The estimate is subtracted from $d(t)$, forming an error signal, $e(t)$. The LMS algorithm steps along the error surface to a point where the mean square error (MSE) is minimized, i.e., where the estimate most closely resembles the noise present in $d(t)$. The weight vector is computed with each iteration according to the equation

$$w_r^{(q)}(\tau) = w_r^{(q-1)}(\tau) + \mu \cdot \left(-\Delta w_r^{(q)}(\tau) \right), \quad (3)$$

where μ represents the step size, and $\Delta w_r^{(q)}(\tau)$, the weight vector update for the r th reference channel, which approximates the gradient function of the error surface at τ on the q th iteration. The weight vector update is computed by correlating the error signal, $e(t)$, with the reference noise signal, $N_r(t)$. This corresponds to the steepest descent algorithm, a subset of LMS. However, contrary to the LMS and steepest descent algorithms, in AJOB, $w_r^{(q)}(\tau)$ remains constant while $\Delta w_r^{(q)}(\tau)$ is being computed. This is better known as “block-LMS.” Its advantage over classical LMS is reduced noise in the weight vector update. The value of the weight vector update on the q th iteration for the r th reference channel is expressed as

$$\Delta w_r^{(q)}(\tau) = \int_{(q-1)T_{int}}^{(q)T_{int}} e(t) \cdot N_r(t - \tau) dt, \quad (4)$$

where τ is the delay variable, and T_{int} is the integration time, during which the weight vector remains unchanged.

The weight vector update is summed with the weight vector from the previous iteration to form the new weight vector, $w_r^{(q)}(\tau)$, according to Equation (3). Every element in the weight vector corresponds to a unique delay at the delay line. Thus, the product of each weight vector element with the appropriate delay produces a convolution. On the q th iteration, the sum over all R reference noise channels of these convolution results produces the estimate, $y^{(q)}(t)$, to the noise term in the main channel, where

$$y^{(q)}(t) = \sum_{r=0}^R \int_{T_{proc}}^{T+T_{proc}} (w_r^{(q)}(\tau) \cdot N_r(t-\tau)) d\tau. \quad (5)$$

Here, T is the temporal length of each delay line, and T_{proc} is the processing time for the computer to collect the integration data, add the weight vector update to the previously stored values, and to establish communication with the delay line. Then $y^{(q)}(t)$ is subtracted from $d(t)$ to form the error signal in Equation 4 and the next iteration begins. Iterations continue until the algorithm has converged to a solution.

For the experimental implementation of the AJOB system, the integration time, T_{int} , is on the order of milliseconds. With this long integration time, the estimate of the correlation given in Equation (4) is very good and satisfactory convergence results in a single iteration. For this case, the error signal need not be fed back to the correlator, and the correlator can therefore process the main and auxiliary channels directly [6].

3.0 AJOB System Design Considerations

3.1 Overall Considerations

Table 1 shows the short and long term design requirements for the AJOB system. The long term goals reflect requirements for an operational system while the short term goals reflect a proof-of-concept system able to demonstrate the feasibility of optically based adaptive jamming cancellation.

Requirements	Long Term	Short Term
Cancellation Ratio	40 dB	30 dB
Number of Jammers	4	2
Multipath Delay	20 μ sec	5 μ sec
Loop-Lock Time	5 msec	500 msec
System Bandwidth	10 MHz	10 MHz
No. of Multipath Delays	> 4	2

Table 1. Short and long term design requirements.

The AJOB system, as previously mentioned, is designed to provide two processing channels which demonstrate 30 dB cancellation of a 10 MHz bandwidth noise source at a C-band radar IF of 80 MHz. The system consists of four major components: a multichannel optical time-integrating correlator, a digital computer used as an interim signal processor, an acousto-optic tap delay line (AOTDL) filter, and a single-loop electronic canceller. Figure 3 illustrates the AJOB subsystems and their relevant inputs and outputs (two auxiliary antenna inputs and the main channel received signal, $d(t)$). The AO time-integrating correlator accepts the main channel signal and the auxiliary channel signals and performs the appropriate cross-correlations. Using this cross-

correlation information, the PC interface selects the weights applied to the AOTDL filter. The AOTDL filter convolves the auxiliary channel inputs with the weights and sums the resultant channels for an estimate of the jamming signal in the main channel. This was originally subtracted from the main channel to generate the error signal. After the system was further developed, it was noted that it maintained a stable tap position relative to the modulation envelope, but relative to the 80 MHz IF there was phase drift. Therefore, a single-loop electronic canceller was fabricated and inserted into the system at the AOTDL filter output. This, in effect, locks the AOTDL filter output carrier to the main channel signal, thereby achieving effective cancellation. The sections to follow will further detail the presently used system components and possible replacements for better system performance.

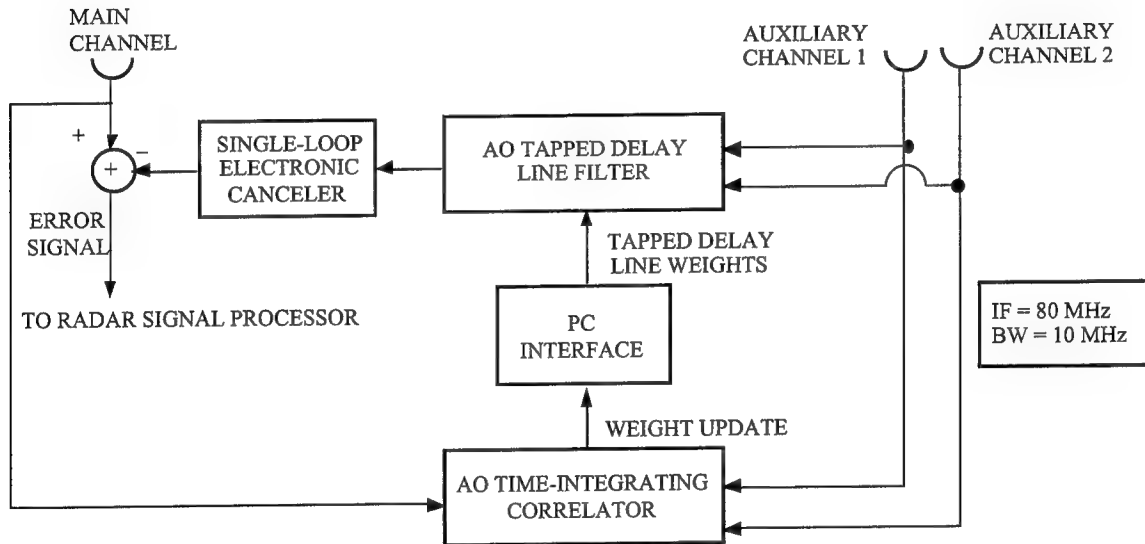


Figure 3. AJOB system layout for two channels.

3.2 Time-Integrating Correlator

Hardware implementation of the steepest descent algorithm as applied to multichannel adaptive optical jamming cancellation, requires the real-time correlation of

wide bandwidth signals from multiple input channels. For many years, optical time-integrating correlators have been studied ([8], [9], [10]) for their potential application to such computational tasks as in Equation 4. The correlator architectures presently competing for use in the AJOB are AO based, consisting of two AO cells (AO1 and AO2).

The correlator receives the main antenna signal and the signals from up to eight auxiliary antennas then finds the location, in time, and the amplitude of the noise in the radar return. Turning to the overall correlation system architecture, the reference input into the system (AO1) is represented by

$$r(t) = A_r(t)e^{j\phi_r(t)}, \quad (6)$$

where $A_r(t)$ and $\phi_r(t)$ are the magnitude and phase of the input reference. The unknown signal input is represented by

$$s(t) = A_s(t)e^{j\phi_s(t)}, \quad (7)$$

where $A_s(t)$ and $\phi_s(t)$ are the magnitude and phase of the input signal. The +1 diffracted amplitude, $R(t)$, from the reference AO cell is given by

$$R\left(t + \frac{x}{v}\right) = r\left(t + \frac{x}{v}\right)e^{j2\pi f_i\left(t + \frac{x}{v}\right)}, \quad (8)$$

and the +1 diffracted amplitude, $S(t)$, from the counterpropagating signal AO cell is given by

$$S\left(t - \frac{x}{v}\right) = s\left(t - \frac{x}{v}\right)e^{j2\pi f_i\left(t - \frac{x}{v}\right)}, \quad (9)$$

where x is the coordinate in the signal AO cell's acoustic propagation direction, v is the acoustic velocity, and f_i is the system input frequency. The beam produced by $R(t)$ in AO1 is combined with the beam produced by $S(t)$ in AO2 onto a CCD array. The

incident intensity at the CCD array is square-law detected and time integrated to produce the desired correlation.

The voltage output, $V(x)$, from the detector array is the correlation between the reference and signal inputs, and is given by

$$V(x) = \int_0^{T_{\text{int}}} \left| R\left(t + \frac{x}{v}\right) e^{-j2\pi\alpha x} + S\left(t - \frac{x}{v}\right) \right|^2 dt, \quad (10)$$

where T_{int} is the integration time of the detector array and $e^{-j2\pi\alpha x}$ is a phase term caused by the spatial shift of the diffracted order from AO1 passing through a prism. The correlator designs discussed in the next section each use a different medium for control of the spatial frequency of the diffracted order passing through it, but each medium, in general, causes a spatial shift of the light. Insertion of Equations (8) and (9) into Equation (10) yields the voltage output $V(x)$ from the detector array

$$V(x) = \text{Low Frequency Biases} + 2\text{Re} \left(e^{-j2\pi\left(\frac{2f_i}{v} - \alpha\right)x} \int_0^{T_{\text{int}}} S\left(t - \frac{x}{v}\right) R^*\left(t + \frac{x}{v}\right) dt \right). \quad (11)$$

As shown in this equation, the correlation is modulated by a spatial carrier and the reference input and signal input are counterpropagating. By noting that x/v is the delay variable, one can see that the detector output is used to create the weight update function as expressed in Equation (4) [11]. The competing subsystems are a Mach-Zehnder and an in-line interferometric architecture.

3.2.1 Mach-Zehnder Time-Integrating Correlator

The Mach-Zehnder time-integrating correlator, shown in Figure 4, relies on interference between the signal beam and the reference beam to form a correlation intensity pattern. A CW laser is split into two optical paths, with an AO cell in each path. During AJOB operational use, one cell is driven by the main radar antenna signal

and the second cell is driven by the auxiliary antennas. With its multichannel AO cells, this correlator has the capability of simultaneously computing the cross-correlation of up to eight auxiliary input signals with an error (main channel) signal.

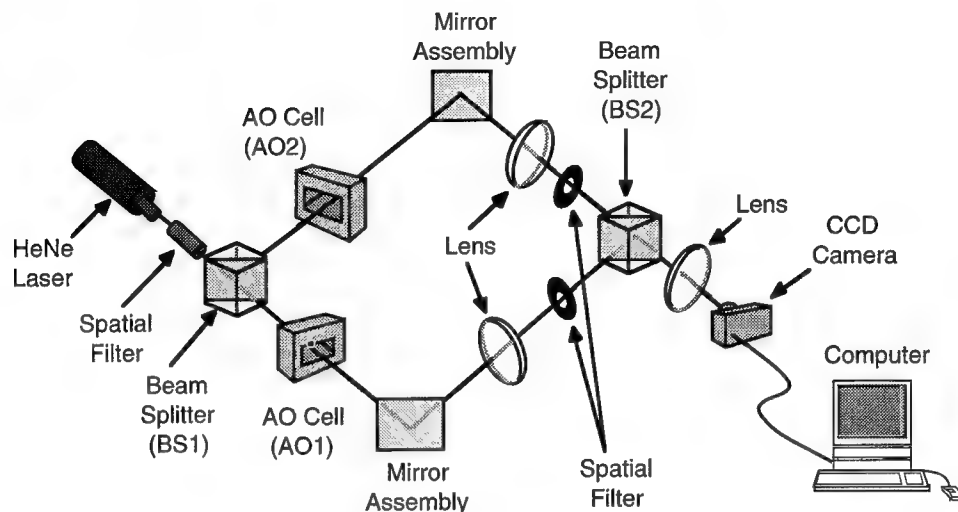


Figure 4. Mach-Zehnder interferometric time-integrating correlator. *The correlator uses an interferometer to set up a stationary spatial intensity pattern. Counterpropagating AO cells perform the correlation.*

The Mach-Zehnder interferometric time-integrating correlator performs the computation of the correlation from Equation (4) in a straightforward manner. Referring to Figure 5, we see an RF carrier modulated by a square pulse as the input to an AO cell. The pulse acts as a diffraction grating propagating through the cell with velocity $+v_a$. Only the light which interacts with this moving grating is diffracted into the +1 order. As the pulse moves, so does the portion of light which is diffracted. This causes a spot to scan across the CCD array with velocity $-v_a$. Now the same RF signal is introduced into a second AO cell in a counterpropagating direction, i.e., with velocity $-v_a$. Through the same process just described, this produces a second scanning spot which moves across the CCD array with velocity $+v_a$.

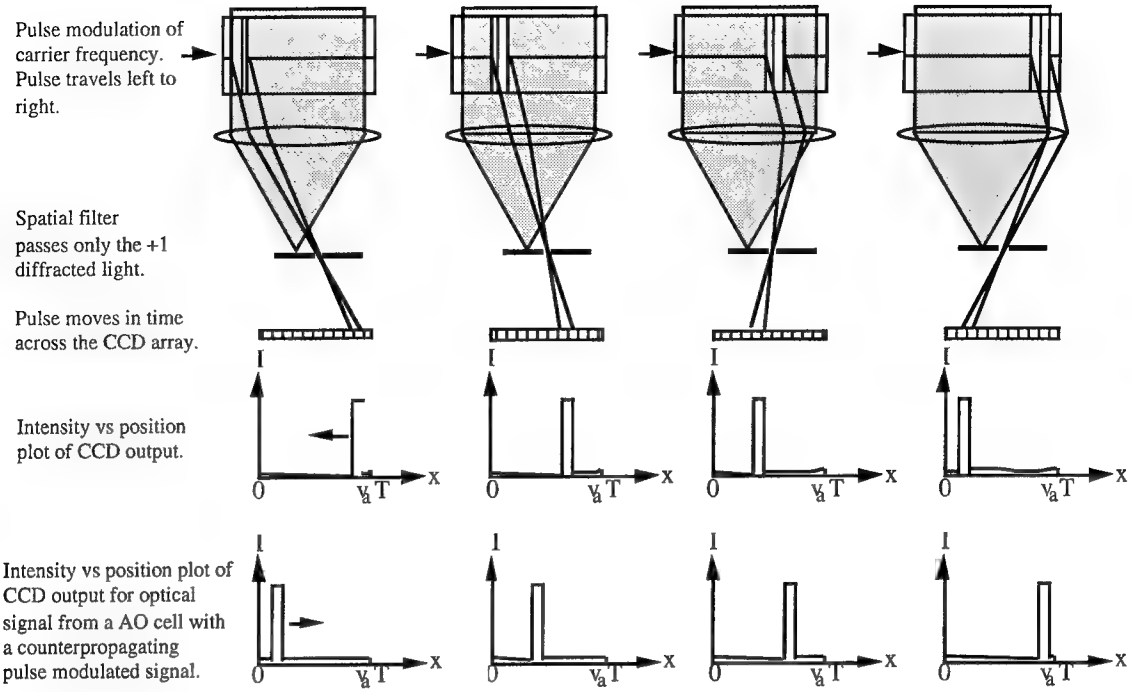


Figure 5: Conceptual diagram of autocorrelation with Mach-Zehnder time-integrating correlator. *The AO cells in the correlator are oriented so that the acoustic pulses counterpropagate. These counterpropagating pulses create counterpropagating optical beams which sweep by one another and build up the intensity pattern on the CCD array. The time integrated CCD output represents the correlation between the two RF input signals.*

These two scanning spots move in opposite directions on the CCD array with equal speed. The CCD array integrates for a time, T_{int} , during which the scanning spots pass over one another many times. The light intensity builds up on the CCD array in the region of overlap. Since the scanning spots are at the same optical frequency, they produce interference fringes [12]. The fringe spacing, which serves as a spatial carrier here, may be adjusted through rotation of the beamsplitter BS2 [3].

A problem encountered with the Mach-Zehnder correlator during testing [11] was vibration sensitivity. To address this issue, a modified version of Riza's [13] correlator architecture, which uses a common path interferometer in combination with an in-line configuration of two counterpropagating AO cells was built and tested [14].

3.2.2 In-Line Time-Integrating Correlator

The interferometric in-line architecture, shown in Fig. 6, consists of imaging the +1 diffracted order and undiffracted light from a reference AO cell (AO1) onto a second AO cell (AO2) which is driven by an unknown signal. AO2 is oriented so as to satisfy the Bragg condition for the undiffracted light from AO1. The imaging process ensures the +1 diffracted order from AO1 overlaps the +1 diffracted order from AO2. A CCD array integrates the light in this overlap region, exactly like the Mach-Zehnder correlator, thus forming the correlation of the reference with the unknown signal. The inclusion of the Dove prism is necessary because the imaging system between the two AO cells inverts not only the angular deflection of the +1 order, but also the propagation direction of the intensity distribution. The effect causes the +1 diffracted orders to move in the same direction, rather than counterpropagate, at the detector plane. The Dove prism not only inverts the effective propagation of the acoustic wave, but it can also be used to cause the beam to undergo a slight angular displacement relative to the +1 order from AO2. This produces interference fringes at the detector plane. The spacing of these interference fringes increases with increased angular displacement between the two diffracted orders.

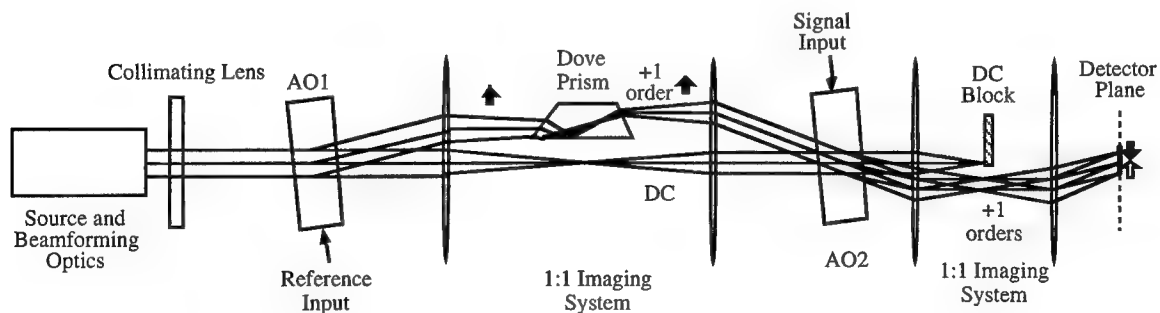


Figure 6. In-line interferometric time-integrating correlator. *Note that the inclusion of the Dove prism ensures counterpropagation of the +1 diffracted orders at the detector and causes an angular displacement between the two diffracted orders.*

The spatial frequency of the fringes produced by the Mach-Zehnder interferometer is tunable by rotating the recombining beamsplitter [11], but this approach suffers from sensitivity to vibrations because of the separated paths of light necessary to form the interferometer, as mentioned. For a non-interferometric in-line correlator, the spatial frequency is a function of the input signal's center frequency. The correlator's useful input signal frequency is limited by the photodetector array pitch. An electronic reference can be used to change the spatial frequency of the correlation, however, this requires additional electronics and adds to the system complexity [10]. For these reasons, the above in-line architecture offers advantages useful for adaptive processing.

The geometry of the Dove prism and how its translation along the x-axis affects the correlation spatial frequency will now be examined. A technique for representing the spatial frequency caused by the angular displacement between the two diffracted orders will be found. First, the relationship between the height of the beam entering the Dove prism, P_1 , and the height of the beam exiting the prism, P_2 will be examined. Figure 7 represents the prism and will aid in finding a relationship between P_1 and P_2 .

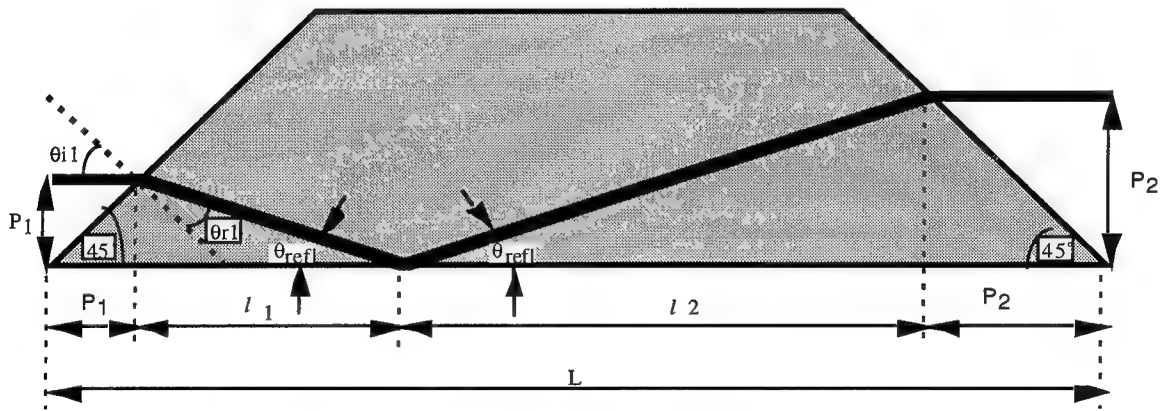


Figure 7. The Dove prism. *The geometry of the Dove prism showing the relationship between P_1 , the height of the beam entering the prism, and P_2 , the height of the beam exiting the prism.*

Referring to Figure 7, note that θ_{i1} , the angle of the incident beam, as measured from a normal to the entrance face of the prism is 45° . Using Snell's Law, θ_{r1} , the refracted angle of the beam can be found, after the first interface,

$$n_a \sin \theta_{i1} = n_g \sin \theta_{r1} . \quad (12)$$

Knowing that the index of refraction in air is 1 and in the prism is 1.5, θ_{r1} is 28.1255 degrees. Using simple geometry, the reflected angle measured from the prism base θ_{refl} , is calculated to be 16.8745 degrees. Now, l_1 , the distance to the reflection point, in terms of P_1 , is

$$l_1 = \frac{P_1}{\tan \theta_{\text{refl}}} = \frac{P_1}{0.30334} . \quad (13)$$

Because the reflected angle is symmetric, l_2 , the distance to the exit surface from the reflection point, can be found, and hence P_2

$$\frac{P_2}{l_2} = \frac{P_1}{l_1} , \text{ and} \quad (14)$$

$$L = P_1 + l_1 + P_2 + l_2 , \text{ so} \quad (15)$$

$$l_2 = \frac{L - P_1 - l_1}{\left(\frac{P_1}{l_1} + 1 \right)} , \text{ and} \quad (16)$$

$$P_2 = \frac{L \cdot P_1 - P_1^2 - l_1 \cdot P_1}{P_1 + l_1} . \quad (17)$$

Substituting Equation (13) into Equation (17) a relationship between P_2 , P_1 , and L can be found,

$$P_2 = \frac{L - 4.2967 \cdot P_1}{4.2967} . \quad (18)$$

Figure 8, which follows the path of the diffracted and undiffracted light from AO1 to AO2, can be used to find the effect of the beam shift caused by the prism. The Bragg angle for AO1 is defined as

$$\theta_B = \frac{\lambda f_i}{2v}, \quad (19)$$

where θ_B is the Bragg angle, λ is the optical wavelength, and v is the acoustic velocity in the AO cell. The separation between the undiffracted (DC order) and the +1 diffracted order is twice that of the Bragg angle, so the height, H_1 , in Figure 8 is

$$H_1 = \tan \theta_1 \cdot f_{L1} = \tan \left(\frac{\lambda f_i}{v} \right) \cdot f_{L1}. \quad (20)$$

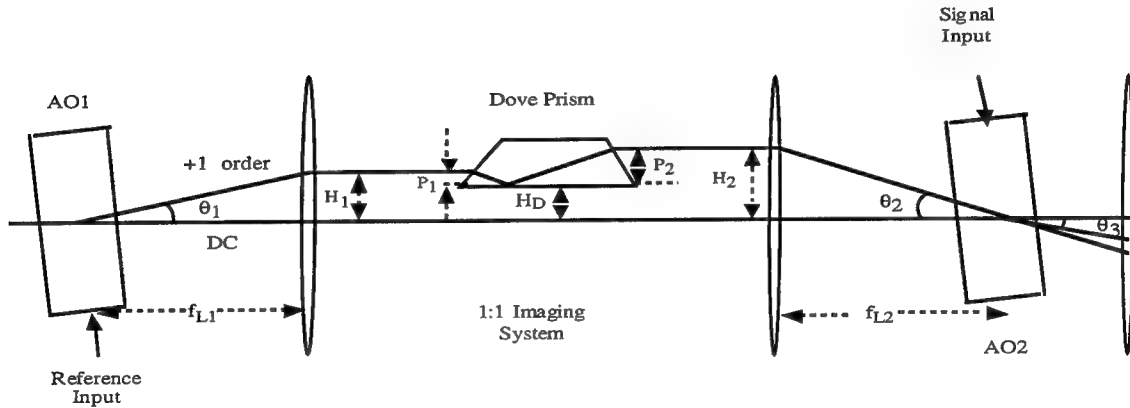


Figure 8. Paths of diffracted and undiffracted light from AO1 to AO2.

There is a distance, from the base of the prism to a height, H , over which the Dove prism is useful for tuning the spatial frequency. This height H is the distance from the base of the prism to that point on the prism which will make P_1 equal to P_2 . Referencing Figure 7, when P_1 equals P_2 there will be no beam shift and no induced spatial interference fringes at the detector. There is enough information from the Dove prism analysis to solve for H in terms of the length of the base of the prism, L . Referring to Figure 7, the conditions for $H = P_1 = P_2$ occur when the beam hits the prism base at a point one-half

the length of prism base. Since $P_1 + l_1 = 0.5 L$, substituting H for P_1 and using Equation (13),

$$H = 0.1164L. \quad (21)$$

To maximize the correlator's bandwidth, we would like the diffracted beam corresponding to the center frequency of operation to enter the prism at $H/2$ or $0.0582L$. Referring to Figure 8, the distance from the undiffracted light to the base of the prism, H_D , at the center frequency, f_c , is found using Equations (15) and (16) by solving the relationship $H_D = H_1 - P_1$

$$H_D = \tan\left(\frac{\lambda f_c}{v}\right) \cdot f_{L1} - 0.0582L. \quad (22)$$

The height of the beam entering the Dove prism can now be found for any frequency with respect to the system center frequency by subtracting H_D from H_1 . Solving for P_1 as a function of input frequency f_i we obtain

$$P_1(f_i) = \tan\left(\frac{\lambda f_i}{v}\right) \cdot f_{L1} - \left[\tan\left(\frac{\lambda f_c}{v}\right) \cdot f_{L1} - 0.0582L \right]. \quad (23)$$

Substituting variables in Equation (18) we can now write $P_2(f_i)$ as

$$P_2(f_i) = 0.1745L - \tan\left(\frac{\lambda f_i}{v}\right) \cdot f_{L1} + \tan\left(\frac{\lambda f_c}{v}\right) \cdot f_{L1}. \quad (24)$$

Now that we know the height, from the prism base, of the diffracted beam exiting the prism, we can find H_2 , the distance between the diffracted and undiffracted orders, by observing, in Figure 8, that

$$H_2 = H_D + P_2. \quad (25)$$

The angle of the diffracted order from AO1 will be unaffected when passing through AO2, because AO2 is set to satisfy the Bragg condition of the undiffracted order.

However, due to the spatial shift caused by the Dove prism, θ_2 will differ from θ_1 . We can solve for θ_2 by substituting for variables in Equation (20)

$$\theta_2 = \tan^{-1}\left(\frac{H_2}{f_{L2}}\right), \quad (26)$$

where $f_{L2}=f_{L1}$ due to the 1:1 imaging system. The angle, θ_3 , of the light diffracted from AO2 is equal to θ_1 because both AO cells operate at the same input frequency. With this in mind, we are able to calculate the spatial frequency caused by the angular displacement between the two diffracted orders. If we define θ_D as the difference in the two diffracted orders, the spatial frequency α is defined as

$$\alpha = \frac{\theta_D}{\lambda} = \frac{\theta_2 - \theta_3}{\lambda} = \frac{\tan^{-1}\left(\frac{H_2}{f_{L2}}\right) - \frac{\lambda f_i}{v}}{\lambda}. \quad (27)$$

Using Equation (24) to find the exit height of the diffracted order from the prism we solve Equation (27) to find the spatial frequency caused by the angular displacement of the diffracted orders. The resultant spatial frequency is described in terms of the center frequency, input frequency, focal length of the imaging lenses, and the base length of the Dove prism. The fringe spacing at the detector is equal to the inverse of the spatial frequency, for a 1:1 imaging onto the detector plane. The magnification of the imaging system onto the detector will alter the fringe spacing by the magnification factor [15]. Figure 9 shows calculated results for fringe spacing of various focal length lenses versus input frequency into the system. The calculations were performed for a Dove prism of $L = 20$ mm and for $f_c = 80$ MHz. As can be seen, the fringe spacing increases with increased focal length lenses and increased input frequency. The position of the Dove prism, H_D , with respect to the undiffracted order is approximately $25 \mu\text{m}$ at a focal length of 100 mm, which is impractical for system design. Focal length lenses of 200 mm give a H_D of 1.2 mm, and provide adequate fringe spacing across the 40 MHz bandwidth when using a detector pitch of $26 \mu\text{m}$.

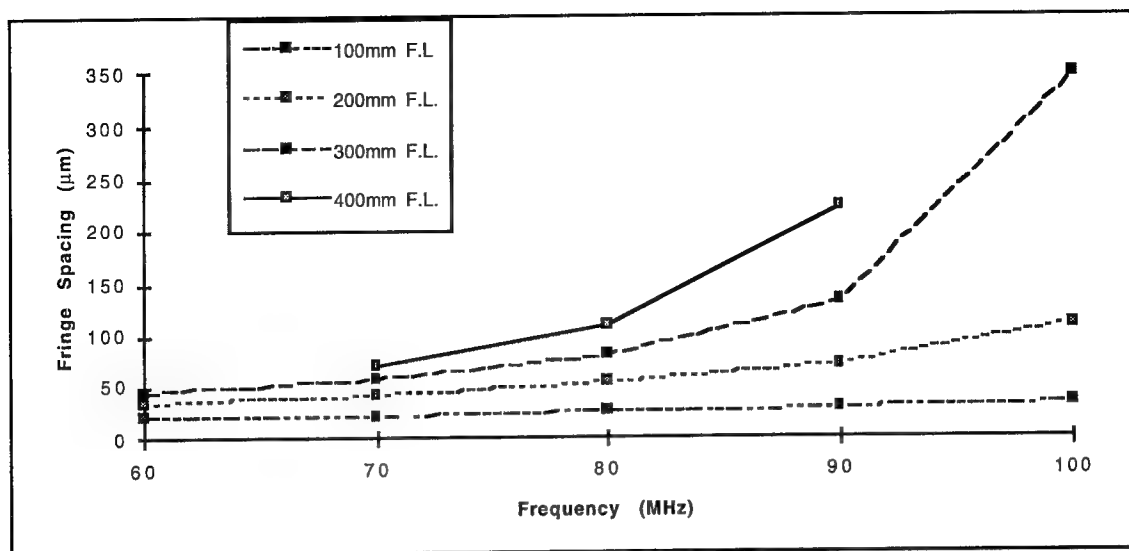


Figure 9. Fringe spacing versus input frequency for various focal length lenses. *The Dove prism used has base length of 20 mm and the system center frequency is 80 MHz.*

3.2.3 Mach-Zehnder Experimental Setup

The layout for the Mach-Zehnder interferometric correlator is shown in Figure 10. This layout was built and tested under contract with Dynetics, Inc. of Huntsville, Alabama [4]. Light from a 14 mW continuous wave HeNe laser at 632.8 nm was used as the reference beam. The reference beam is spatially filtered and then collimated by a 200 mm focal length achromat. Achromats were used for minimum aberrations and wavefront distortions. The collimated light is split by a beamsplitting cube into two separate paths. Each path contains an AO cell exactly like the ones used in the in-line correlator. The multichannel AO cells are 8-channel, TeO_2 longitudinal-mode deflectors manufactured by Brimrose Corporation. The deflectors have a 5 μsec time aperture and a 30 MHz bandwidth centered at 80 MHz. The counterpropagating +1 diffracted orders and the undiffracted DC light, produced by AO1 and AO2, are then recombined by a second beamsplitting cube. Recall that the spatial frequency of the fringes produced is tunable at this second beam splitting cube. The beamsplitting cubes are securely mounted between two plates to aid in the reduction of vibrations. An imaging system, consisting of a 200

mm focal length achromat and a 50 mm focal length cylindrical lens, images the counterpropagating +1 diffracted orders onto the detector plane. A DC block, located at the focal plane of the system, prevents the undiffracted DC light from illuminating the detector. The cylindrical lens was used to collapse the interference fringes onto the detector array in order to obtain a more uniform distribution across the array. The resulting interference is then integrated with respect to time, thus forming the correlation of the two input reference signals.

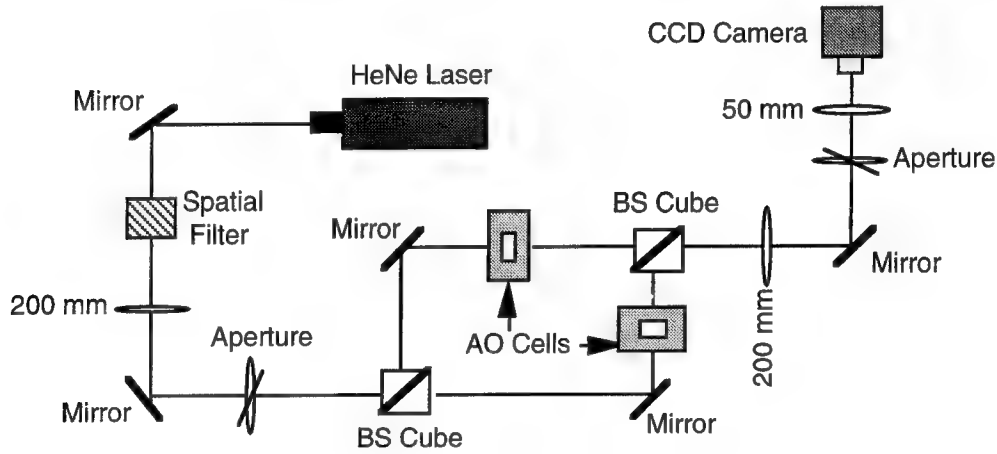


Figure 10. Mach-Zehnder time-integrating correlator experimental layout.

3.2.4 In-Line Time-Integrating Correlator Experimental Setup

Figure 11 shows the experimental layout for the in-line architecture. A spiral design was used to enable the correlator to fit on a 2 ft. by 2 ft. optical table. We used a 14 mW HeNe laser at 632.8 nm which is spatially filtered and collimated by a 200 mm focal length achromat. The first imaging system consists of two 300 mm focal length achromats. The collimated light passes through the first AO cell and produces a DC and a +1 diffracted order, due to an input signal to the AO cell on an 80 MHz carrier. At the focal point of this first imaging system is the Dove prism. The prism is mounted on an x-translation stage and positioned so that the +1 order passes through it and the DC light is

unaffected. The Dove prism has a base length of 20 mm. As discussed, the spatial displacement induced by the prism results in an angular displacement of the +1 order when it is imaged onto AO2. AO2 is oriented to satisfy the Bragg condition of the DC light. The signal input into AO2 is also on an 80 MHz carrier, but because of the Dove prism, produces a +1 diffracted order which propagates at a slight angle to the +1 order from AO1.

The second imaging system, consisting of one 200 mm and one 100 mm focal length achromat, images the two +1 diffracted orders onto the detector. This imaging system will give half the fringe spacing, at the detector, than would be seen with a 1:1 imaging system. A DC block is used at the focal plane of the second imaging system to allow only the diffracted orders to pass to the detector.

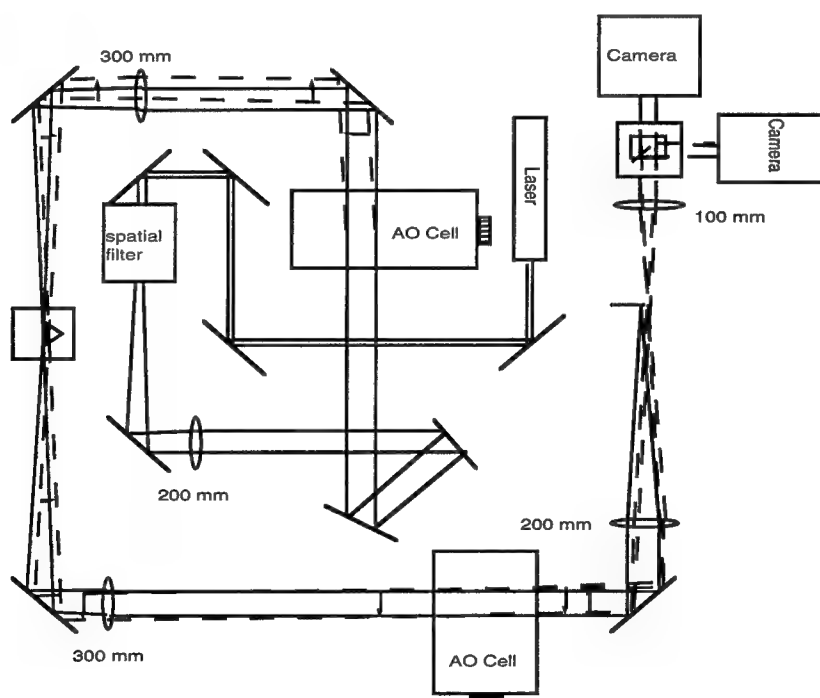


Figure 11. In-line time-integrating correlator experimental layout.

3.3 Interface Techniques

The current interface between the correlator and tapped delay line is a digital computer. The computer continually monitors and updates the correlations and decides where to set tap locations. The use of a digital computer produces inherent limitations on the speed of the system but helps to combine the parallel computation power of optics in tandem with the algorithmic flexibility of a computer. The hardware required to collect the correlation information from the correlator and translate this result into taps on the delay line is shown in Figure 12. The detectors used for the correlator are Reticon LC1901 linear charge-coupled photodiode arrays each with 512 pixels. The arrays are interfaced to a personal computer through a Girard 3197 8-bit A/D converter.

Some of the features gained through the software developed for the AJOB system include correlation display, computer control of various camera parameters (such as integration time), and control of various signal generation devices used to drive the AOSLM in the AOTDL subsystem. An additional feature allows for the subtraction of background amplitude non-uniformities caused by the AO cells and CCD cameras. Background subtraction generates a low-noise signal for processing, thereby improving the correlation results.

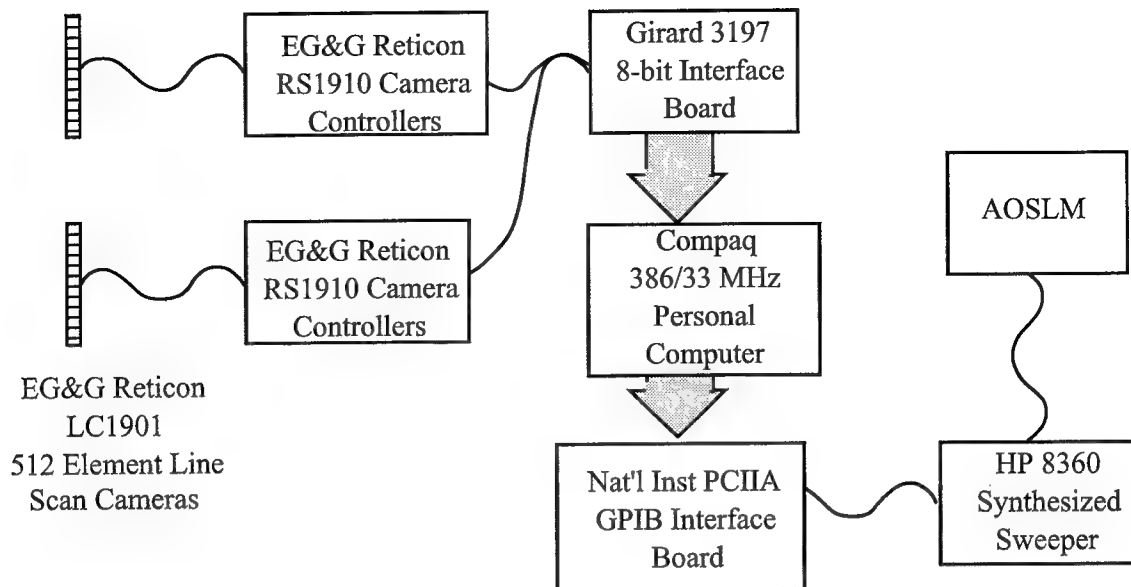


Figure 12. Computer controlled interface. *The line scan cameras collect the correlation data from the time-integrating correlator. The interface shown processes the correlation information and forms optical taps on the AO delay line through the AOSLM.*

3.3.1 Computer Software

The software developed for this project allows for near real time viewing of the correlation results. The hardware/software system retrieves raw correlation data from the CCD camera, cleans and processes this data, and displays the end product on the computer's monitor. This is accomplished at a rate of approximately four frames per second.

The signal cleaning involves two processes. The first is a background subtraction which eliminates many of the amplitude non-uniformities introduced by the optical system. The other cleaning process ensures that, for a given spatial carrier, the amplitude of each carrier peak is essentially constant across the aperture of the CCD array. These results are then extrapolated back to the signal of interest in the hopes of filtering out small scale non-uniformities that are causing erroneous results with the signal processing. Other minor pre-processing measures include introducing a bias level (which is discounted

for the actual signal processing), taking the absolute value of the signal (in order to get a better idea of the true nature of the envelope function), and an average subtraction (to ensure that the absolute value is being taken around the average level of the cleansed signal).

Once the signal is cleansed, the main signal processing takes place. This involves using one of two methods for determining the location of the correlation peak. The first method is a simple search for the highest value of the pre-processed signal. The other method involves fitting the pre-processed data to a triangle and extrapolating the peak of the triangle. This is then used as the correlation peak of the system. During each iteration, peak picking results are averaged with the previous n peaks. This induces stability of the resulting peak by reducing the amplitude of high frequency oscillations. Once the peak is selected for a particular iteration, a calibration factor is introduced and used to form the input to a Hewlett-Packard 83623A Sweep Synthesizer via a GPIB interface. The amplified output of the synthesizer drives the AOSLM. Positional and amplitude information of the correlation peak corresponds to a drive frequency and amplitude, respectively, for the AOSLM.

3.4 Acousto-Optic Tapped Delay Line

The results from the multichannel time-integrating correlator provide the information required to update the tapped delay line filter coefficients (weight functions) to produce an estimate of the received main channel interference that converges to the optimum block-LMS solution. A personal computer, as described in the previous section, accepts the multichannel correlator outputs and forms new weights. These weights, $w_r^{(q)}(\tau)$, must then be applied to their corresponding signals, $N_r(t-\tau)$. This can be accomplished optically by spatially forming optical probe beams which tap positions on an AOTDL for the signal $N_r(t)$.

The method used in the AJOB employs an AOSLM. Each tap position at the AOTDL corresponds to a unique RF frequency, f_j , input to the AOSLM. The AOTDL is placed in the Fourier plane of the AOSLM to map these frequencies, f_j , to the AOTDL tap positions with their corresponding weight amplitudes. Each channel of the multichannel AOSLM taps the corresponding channel of a multichannel AOTDL. The resulting tapped outputs from the AOTDL are combined onto a photodiode to achieve the filtered result in Equation (5).

3.4.1 Tapped Delay Line Experimental Setup

Referring to Figure 13, an Adlas model 200 diode-pumped, frequency doubled (532 nm) Nd:YAG 20 mW source is spatially filtered and collimated with an achromat (to reduce aberrations), generating a 40 mm diameter collimated beam. The beam illuminates the active channels of the AOSLM. The AOSLM device is an 8 channel Brimrose Model MTED-8 acousto-optic deflector with an 80 MHz center frequency, 30 MHz bandwidth, 22 mm spatial aperture, and 5 μ sec time aperture.

Lens L2, located a focal length from the center of the AOSLM, focuses all diffracted beams into the multichannel AOTDL. All the beams are parallel and at the Bragg angle relative to the AOTDL. The AOTDL is a device identical to the AOSLM. A spatial filter blocks undiffracted light from the AOSLM allowing only diffracted light to form taps on the delay line. Lens L3 collimates the diffracted and undiffracted beams from the AOTDL and directs these parallel propagating beams onto a ThorLabs Model DET2 silicon photodiode. The detector is located in the region where the overlap of the diffracted and undiffracted beams is largest. The plano-cylindrical lens Cyl1 focuses the light in the vertical direction into the AOSLM. The light is recollimated in the vertical direction by lens L2. Lens Cyl2 focuses the light vertically into the delay line and lens L3 recollimates the light prior to the photodiode.

As stated, the output from the AO tapped delay line subsystem is the estimate given in Equation (5). This output is subtracted from the main channel signal, by a single-loop electronic canceller to form the error signal. In order to achieve effective cancellation at the system IF, precise alignment and calibration of the tap positions and scale is required. In addition, a very uniform frequency response of the AOTDL subsystem is required to achieve cancellation of wideband signals.

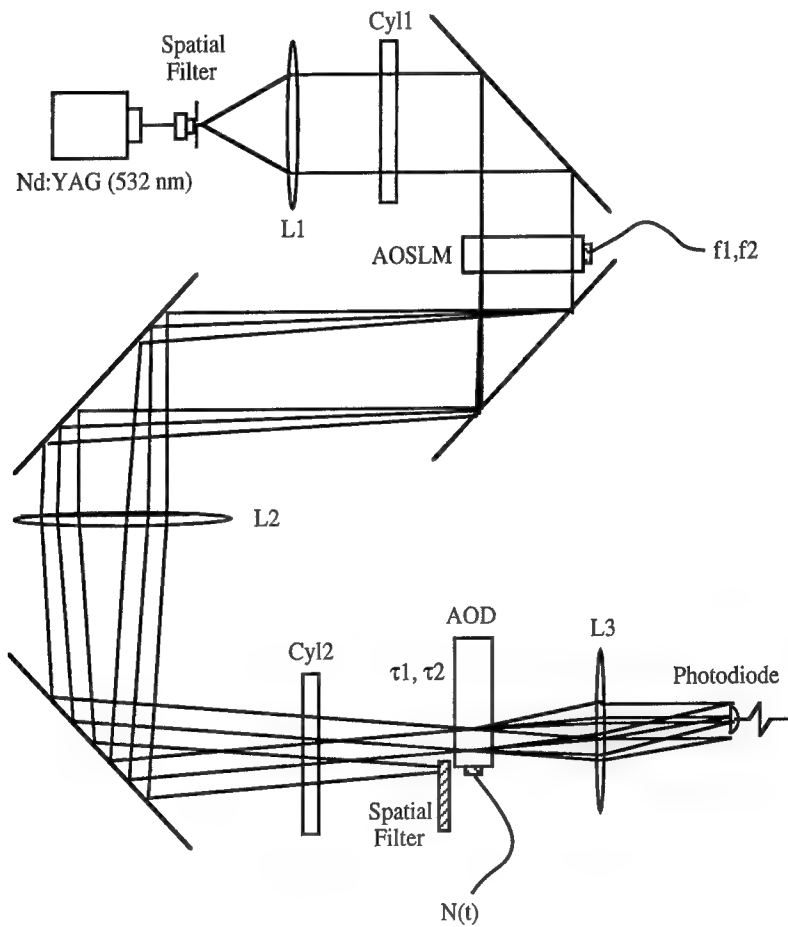


Figure 13. AOSLM used to tap AOTDL. RF frequency inputs f_1 and f_2 generate two diffracted beams which tap the delay line at two corresponding delays, τ_1 and τ_2 .

3.5 Single-Loop Electronic Canceller

In order for the cancellation of the jammer signal to take place in the summer shown in the upper left portion of Figure 3, it is necessary that the carriers be at the same frequency and be phased-locked. In practice this will not occur because of drifts in the optical subsystems supplying the carriers. To circumvent this problem an electronic circuit, called the electronic canceller, was developed, to phase lock the carrier of the AOTDL signal with the main channel signal. This circuit is configured the same as a sidelobe canceller and is shown in Figure 14.

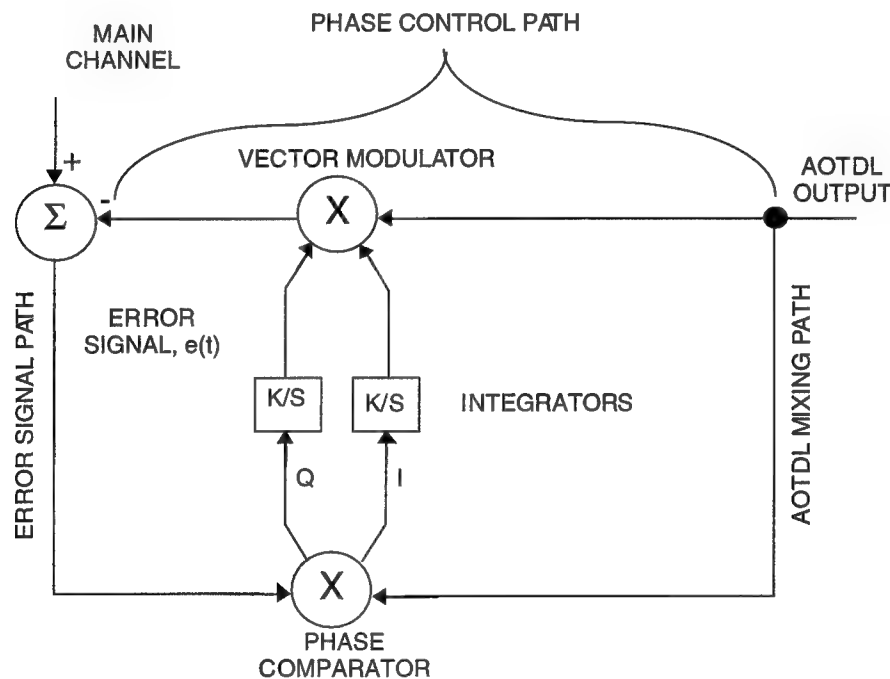


Figure 14. Electronic canceller configuration. *The single-loop electronic canceller phase-locks the AOTDL signal carrier to the carrier of the main channel signal, and then forms an error signal by subtracting the phase-shifted AOTDL signal from the main channel signal.*

The electronic canceller dynamically alters the phase of the AOTDL signal carrier to assure that it is properly phase-locked to the carrier of the main channel signal. An error signal, $e(t)$, is formed by subtracting the phase-shifted AOTDL signal from the main

channel signal. The signal is then mixed with the AOTDL signal to remove the carrier and form a complex, baseband error signal. The in-phase and quadrature (I&Q) components of this error signal are then integrated to form new I&Q signals that define the phase and amplitude adjustment that must be applied to the AOTDL signal to attempt to drive the error signal to zero. If both the main channel and AOTDL signals contain only jammer signals, the error signal will be driven to zero, and the outputs of the phase comparator will also be zero. For the case where the main channel also contains a target signal, the error signal will contain the target signal.

4. Phased Array Radar Tests

The AJOB processor was integrated into Rome Laboratory's Advanced Mainbeam Electronic Counter Counter-Measure (ECCM) Technology Radar and tested during two phases of tests. Phase I occurred 15-26 August 1994 and Phase II occurred 17-28 July 1995. The Advanced Mainbeam ECCM Radar is part of the Surveillance Radar Facility located in Rome, NY. The experimental objectives were to demonstrate AJOB's ability to cancel sidelobe jamming by integrating AJOB into a working radar. The testing made use of the Advanced Mainbeam ECCM Radar's phased array antenna, shown in Figure 15, and a portion of the radar's receive chain. The ground based jammer portion of the facility supplied far-field test signals required for the experiment.

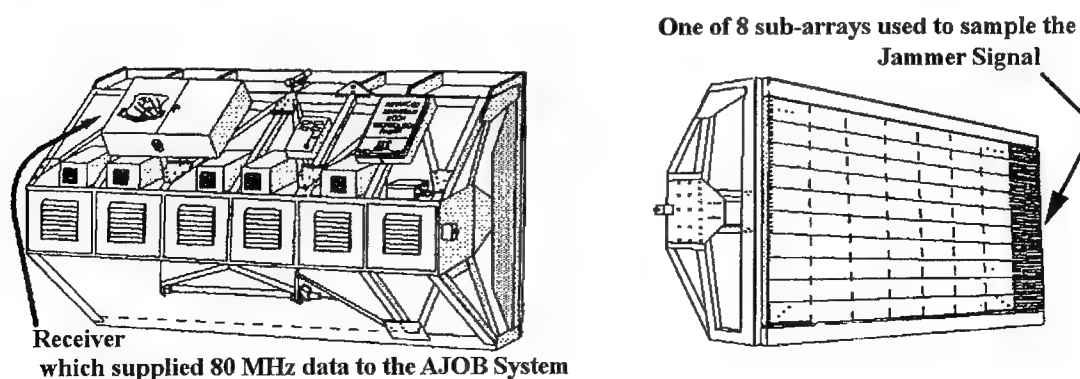


Figure 15. Rome Laboratory ECCM antenna used in live tests.

4.1 Radar Facility Description

The Advanced Mainbeam ECCM Radar was developed during the mid 1980's to implement experimental techniques for rejecting mainbeam interference and noise through the use of adaptive pattern control in both the spatial and polarization domains [16]. This radar is an experimental phased-array radar operating over a tunable frequency band of 5.65 to 5.90 GHz and has an instantaneous bandwidth of 8 MHz. This instantaneous band can be centered at any frequency within the radar's tunable bandwidth. The radar's most unique feature is its antenna which occupies a 12 foot by 6 foot aperture containing 5,120 dual-polarized elements (128 horizontal and 40 vertical). The antenna is electronically scanable ($\pm 45^\circ$) in azimuth and mechanically positionable in azimuth and elevation. The antenna has a sum and difference beam and eight non-overlapping subarrays for each polarization, resulting in 20 beams. The sumbeam's 3 dB beamwidth is one degree in azimuth and two degrees in elevation. Each of the subarrays contains 640 elements (16 horizontal and 40 vertical) yielding a beamwidth of approximately 8 degrees in azimuth.

Each beam of the antenna feeds one of twenty identical receivers with a low noise amplifier front end. These amplifiers set the noise floor for each channel. The signals are then downconverted through a double downconversion scheme to 80 MHz IF. The passband characteristics of each IF channel are governed by a surface acoustic wave (SAW) filter. By shaping the IF passband, this SAW filter sets the intrinsic channel matching level between channels and thereby limits the obtainable wideband cancellation performance. The 3 dB bandwidth of these filters is 8 MHz. The AJOB system was integrated into the radar at this IF stage in the receive chain.

The signals provided for the testing emanated from the ground based jammer portion of the Surveillance Radar Facility, shown in Figure 16. The ground jammers are located 6,500 feet from the radar's antenna; this is well outside the antenna's near-field/far-field boundary of 845 feet. For both phases, two jammers were used which are

capable of producing continuous wave (CW), pulsed CW, and wide-band noise with adjustable amplitude. These jammers each feed a four foot parabolic dish antenna oriented in the direction of the radar under test. Viewed from the test radar, the jammers in Phase I were separated by 0.58 degrees in azimuth. In order to achieve more azimuth separation for Phase II testing, the S-Band antenna, Figure 16, was modified to produce a C-Band frequency in order to utilize the 1.16 degree separation between Jammer 1 and the *modified* S-Band antenna.

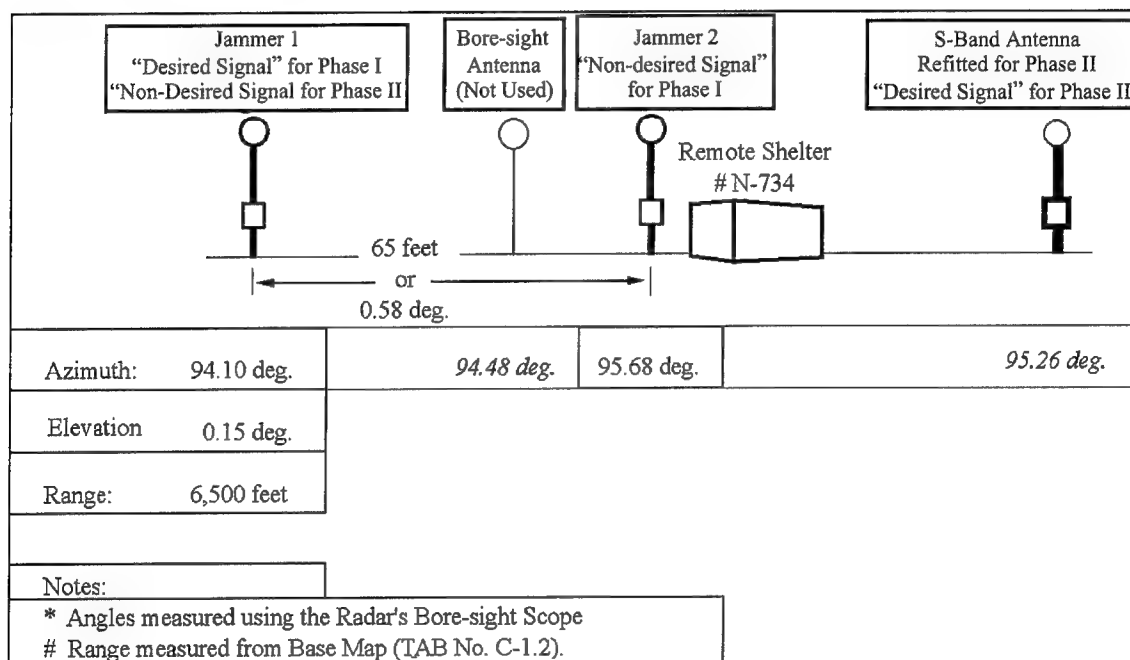


Figure 16. Remote jammer site.

4.2 Test Set-Up

Compatibility between the Advanced Mainbeam ECCM Radar and the AJOB processor made the Surveillance Radar Facility the ideal location for a field test of the processor. The relationship between the radar's main beam and the auxiliary beams furnished by the subarrays allowed for a convenient and predictable experimental configuration. Compatibility of the IF and instantaneous bandwidth, the quality of the IF

receive path, as well as the availability of far-field signal sources all contributed to the success of these experiments. All experiments in connection with the AJOB processor were conducted with the radar in receive-only mode. That is, the radar was not transmitting during the course of any of the experiments and only signals generated from the ground jammer installation were received. This was done to create a controlled economical environment for testing. Using true radar returns would require a controlled aircraft and a controlled jammer. For Phase I Tests, the experiment was performed by configuring Jammer 2 (see Figure 16) as a *non-desired interfering signal* source, and Jammer 1 as the *desired signal source*. The desired signal source was configured to emit CW energy. This signal simulated a radar return of a hostile target. The level of this signal can be adjusted to obtain a desired signal-to-jammer (S/J) ratio and its frequency is set to the center of the radar's band.

During the tests, the non-desired signal source was configured to simulate spot-jamming and barrage noise jamming. Spot-jamming is a self-screening or support electronic counter measure (ECM) technique that radiates narrow-band (CW) noise-like energy that masks expected signal returns of a victim radar [17]. Spot-jamming is employed when the ECM asset can determine the operating frequency of the victim radar and maximizes the in-band jamming energy. For these experiments, a CW signal was used to simulate spot-jamming. The goal of a radar being attacked by a spot noise jammer is to avoid the jamming energy by changing operating frequency, and thus minimize the in-band jamming energy. The ECM asset will attempt to follow the frequency hopping of the victim radar. However, if the victim radar is agile enough, the ECM asset will ultimately be forced into barrage noise mode. Barrage noise is the spreading of noise-like jamming energy over a wide frequency band such that the victim radar is jammed over its entire tunable bandwidth [17]. Barrage noise jamming has the ECM advantage that some of the jamming energy will be in-band, however, the jammer's energy is spread over a larger bandwidth, so the amount of in-band energy is greatly reduced. The bandwidth of this jammer is 25 MHz, centered in the radar's band.

Most of Phase I testing could not achieve the goal of sidelobe radar jamming due to the initial set power levels of the jammer site and the 0.58 degree separation of Jammer 1 and Jammer 2. To compensate, Jammer 1 was attenuated with a thumb-wheel attenuator in order to achieve the proper S/J ratio. This amplitude alignment allowed the last day of Phase I tests to have the radar's mainbeam aim closer to the *desired signal* and properly place the *non-desired interference signal* or Jammer 2 on the sidelobe, see Figure 17. This sidelobe jammer configuration verified the results from the previous Phase I tests. Phase II tests improved the sidelobe configuration by placing the desired signal closer to beam center while still having the non-desired interfering signal on the radar's sidelobe for sidelobe jamming. To achieve this, the S-Band Antenna (in Figure 16) was refitted to become a C-Band frequency desired signal with the appropriate amplification to obtain a desired S/J ratio. Phase II tests achieved land-based sidelobe jamming which validated Phase I test results.

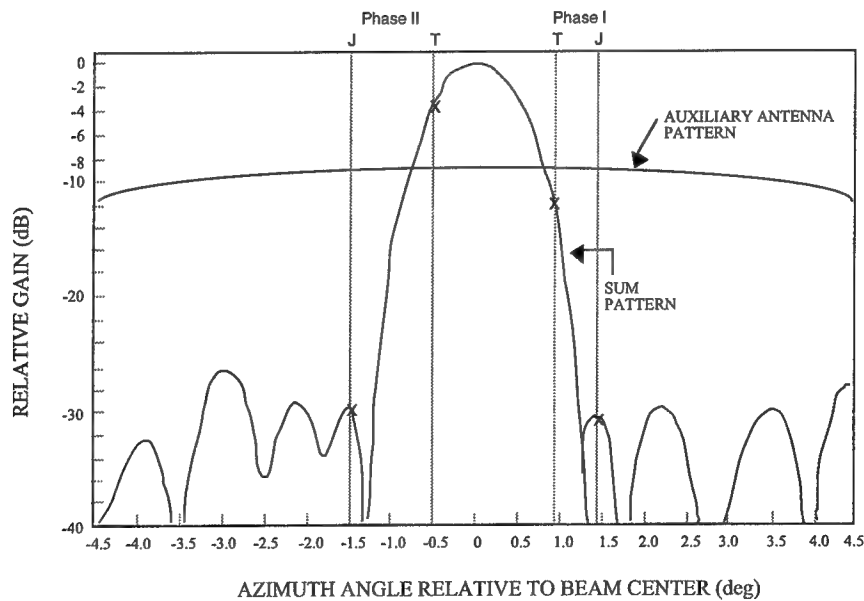


Figure 17. Azimuth antenna patterns showing jammer and target locations. For each phase of testing, the target is located on the mainbeam of the sum pattern and the jammer is located on the sidelobe.

5. Data

The following subsections include data gathered for correlator dynamic range considerations, test results for software based signal processing, AOTDL test results, and finally, radar experimental test results.

5.1 Correlator Architecture Dynamic Range Considerations

An important consideration of any optical system is its useful dynamic range. A dynamic range test setup, shown in Figure 18, was designed under contract with Dynetics, Inc. of Huntsville, Alabama [4]. This signal generation layout was first used to test the Mach-Zehnder correlator and then adopted to test the in-line correlator. The dynamic range test consists of two wideband signals (separated in time) input into AO2 (signal input) while only one wideband signal is input into AO1 (reference input). The output of the correlator is two correlations that are separated by the relative delay between the two signals input into AO2.

During testing, the total power into both AO cells was held relatively constant at approximately 235 mW. The signal generation layout allows for the attenuation of one of the wideband signals into AO2, while maintaining a constant input power. The 100 MHz noise source was filtered, using a 10 MHz bandpass filter centered at 80 MHz. The 10 MHz noise signal was then split, using a three-way splitter, for input into the two AO cells. The signal into AO1 was delayed using an Anderson Labs, Bulk Acoustic Wave (BAW) delay line set at 5.5 μ secs. In the two remaining paths, BAW delay lines of 5' and 6 μ secs were used to delay these two signals by 1 μ sec with respect to each other. The two signals were then combined, using a two way combiner and input into AO2. Figure 19 shows the signals tapped from the test layout by using coupled ports. The top signal is the tapped input into AO1 and the lower signals are those input into AO2. As expected, there is a delay of 1 μ sec between the signals input into AO2, and the signal

input into AO1 is delayed 0.5 μsec with respect to the lower signals. Note that the difference in size of the input signals into each AO cell, as seen in Figure 19, is due to the placement of the coupled ports as shown in Figure 18.

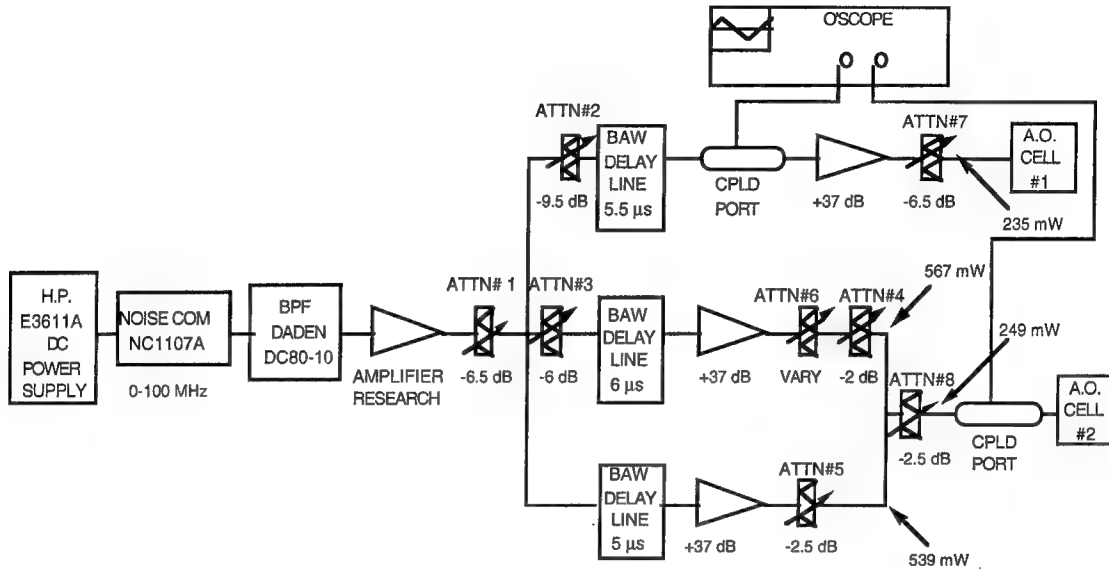


Figure 18. Dynamic range test signal generation layout.

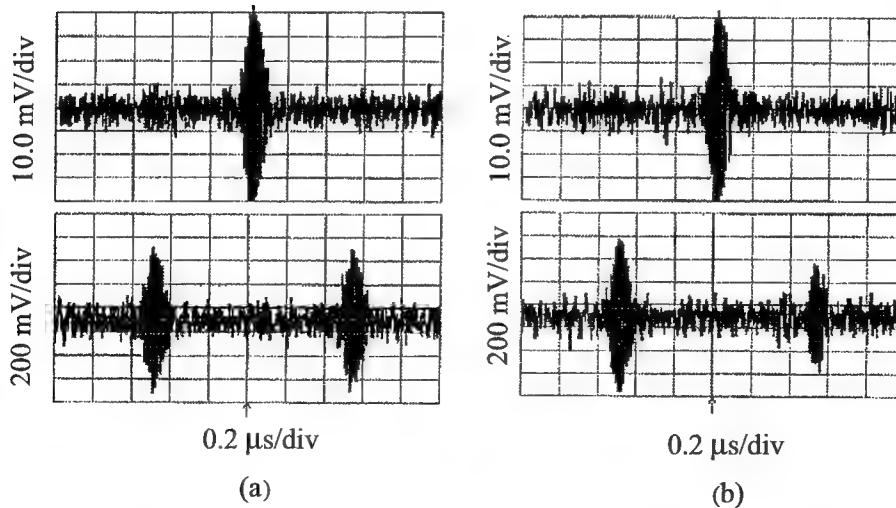


Figure 19. Input signals for dynamic range testing: (a) No attenuation, (b) 3 dB attenuation of the 6 μsec delayed input signal to AO2.

The dynamic range test, as described above, was performed on both the in-line interferometric correlator and the Mach-Zehnder interferometric correlator. The 6 μ sec-delayed signal, input into AO2, was attenuated (using attenuator 6) in 1dB increments. The dynamic range results for the Mach-Zehnder interferometric correlator are depicted in Figures 20, 21, and 22, at attenuation levels of 0, 20, and 27 dB respectively.

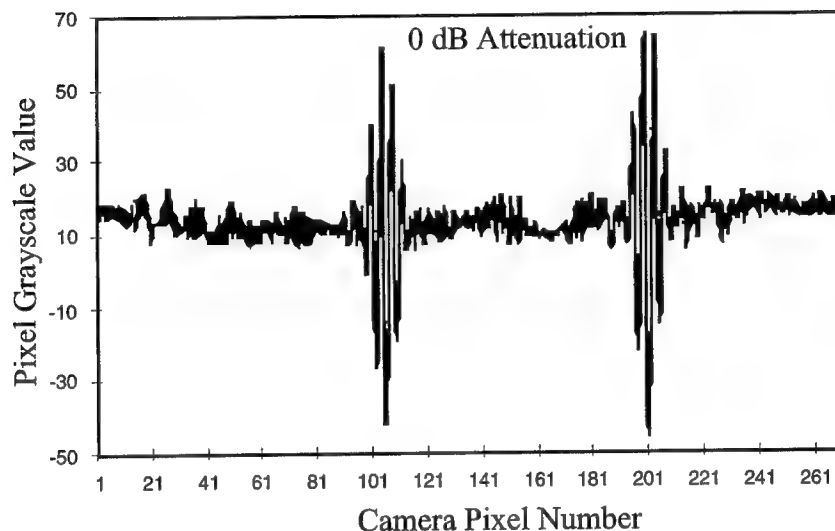


Figure 20. Dynamic range test for Mach-Zehnder correlator at 0 dB attenuation.

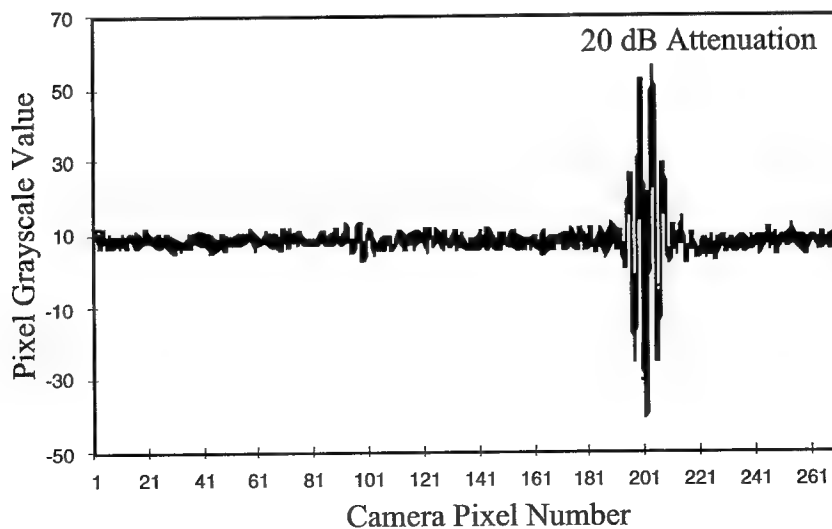


Figure 21. Dynamic range test for Mach-Zehnder correlator at 20 dB attenuation.

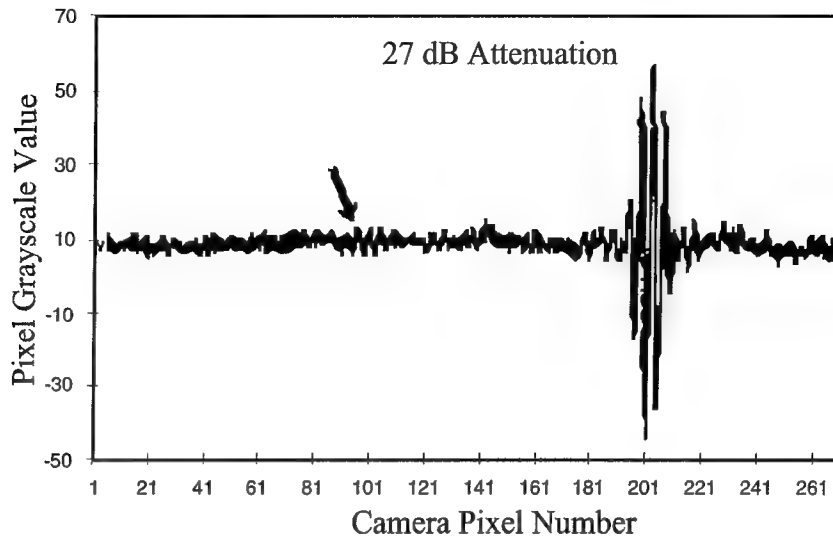


Figure 22. Dynamic range test for Mach-Zehnder correlator at 27 dB attenuation.

The dynamic range results for the in-line interferometric correlator are depicted in Figures 23, 24, and 25 at attenuations of 0, 20, and 29 dB respectively.

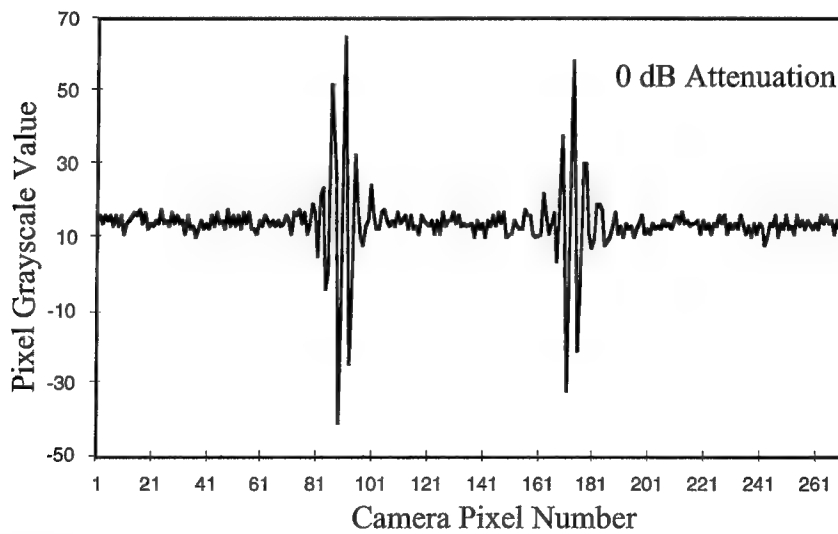


Figure 23. Dynamic range test for in-line correlator at 0 dB attenuation.

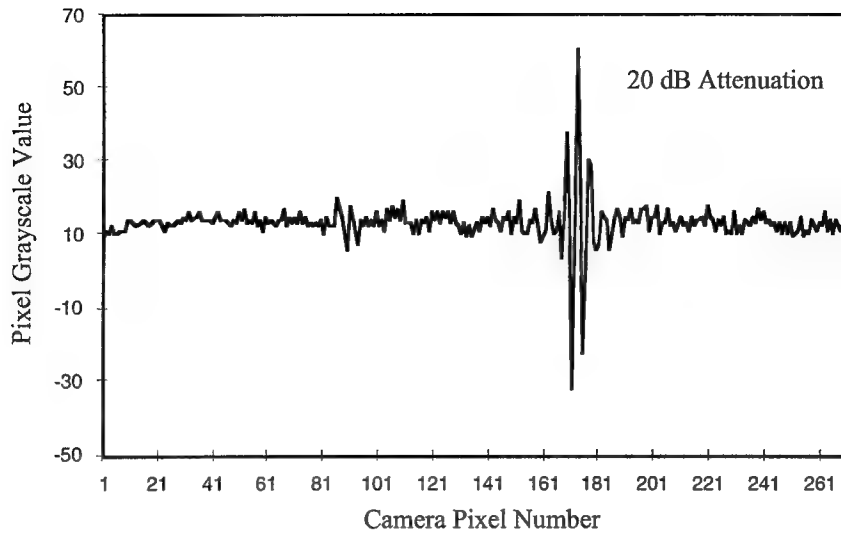


Figure 24. Dynamic range test for in-line correlator at 20 dB attenuation.

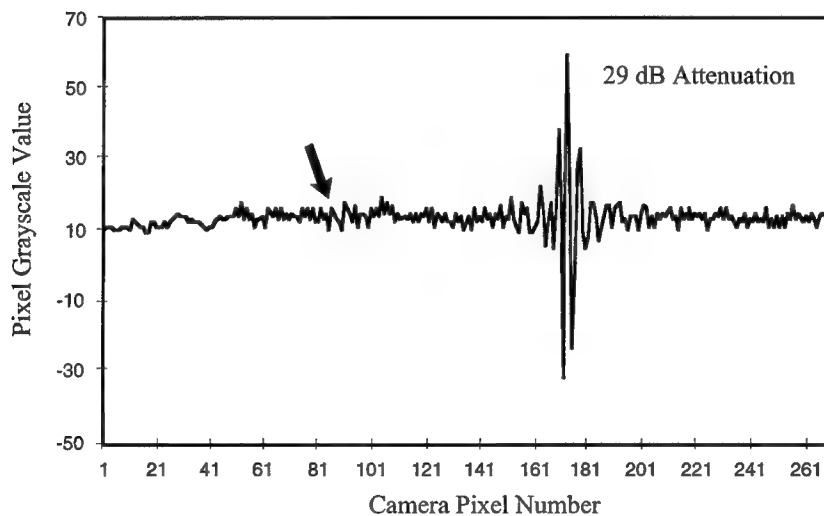


Figure 25. Dynamic range test for in-line correlator at 29 dB attenuation.

The accuracy of the dynamic range tests was limited due to the pixel-to-pixel non-uniformities and the gain imbalances, which occur between the odd and even pixels of the detector. The correlation results became unreadable at attenuations larger than the ones depicted in Figures 22 and 25. Therefore, according to these results, the dynamic range of the in-line correlator appears to be 29 dB, and the dynamic range of the Mach-Zehnder

correlator appears to be 27 dB. Both correlators have been used in radar testing of the AJOB system and indications thus far support a change to the in-line correlator. Vibrational testing will be performed in the future, utilizing a piezoelectric stand, to indicate which architecture best fits the needs of the AJOB system.

5.2 Test Results for Software Based Signal Processing

Figures 26-28 demonstrate the usefulness of the computer. Using the dynamic range layout in Figure 18, we can see the raw data directly collected by the CCD camera, in Figure 26. As can be seen, there are background non-uniformities caused by the AO cells and the CCD camera. Figure 27 shows the subtraction of the background non-uniformities and the removal of the image's bias level (average pixel intensity across the aperture of the camera). To better determine the peak pixel location of the correlation, the computer also subtracts the average of all pixel values from the results of the background non-uniformity subtraction, and takes the absolute value. This is reflected in Figure 28. During system operation this is used to determine the location of the correlation peak. During each iteration, peak picking results are averaged with the previous n peaks. Once the peak is selected for each iteration, a calibration is introduced and used to form the input to a Hewlett-Packard 83623A Sweep Synthesizer via a GPIB interface. The amplified output of the synthesizer drives the AOSLM. Positional and amplitude information of the correlation peak correspond to a drive frequency and amplitude, respectively, for the AOSLM.

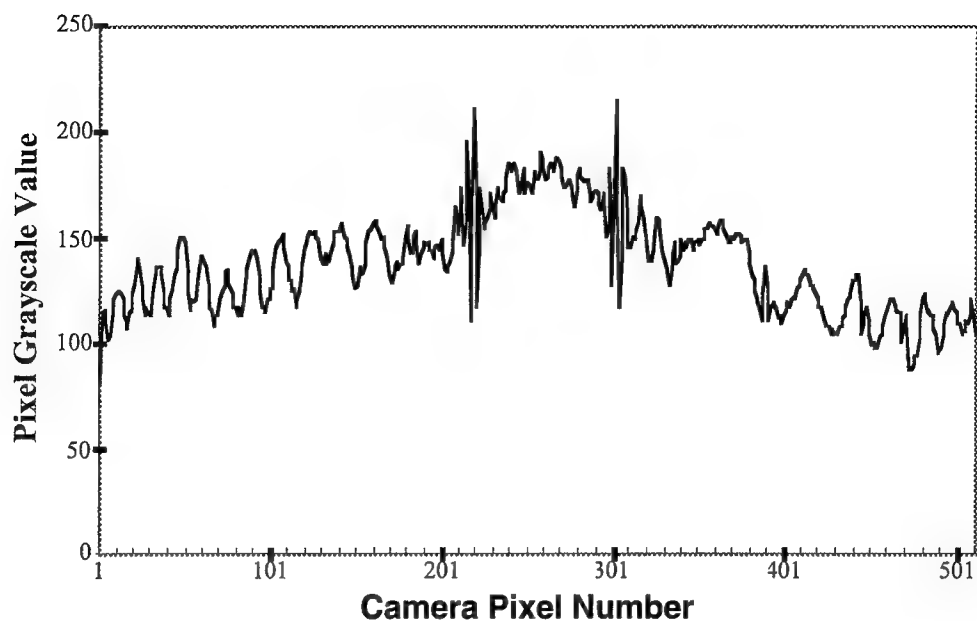


Figure 26. Raw detector output.

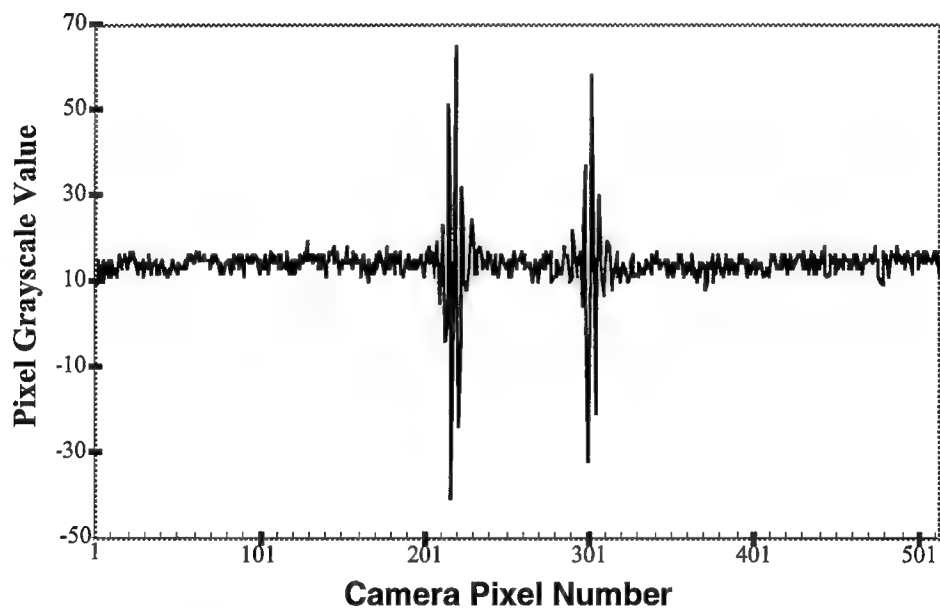


Figure 27. Background non-uniformities subtracted.

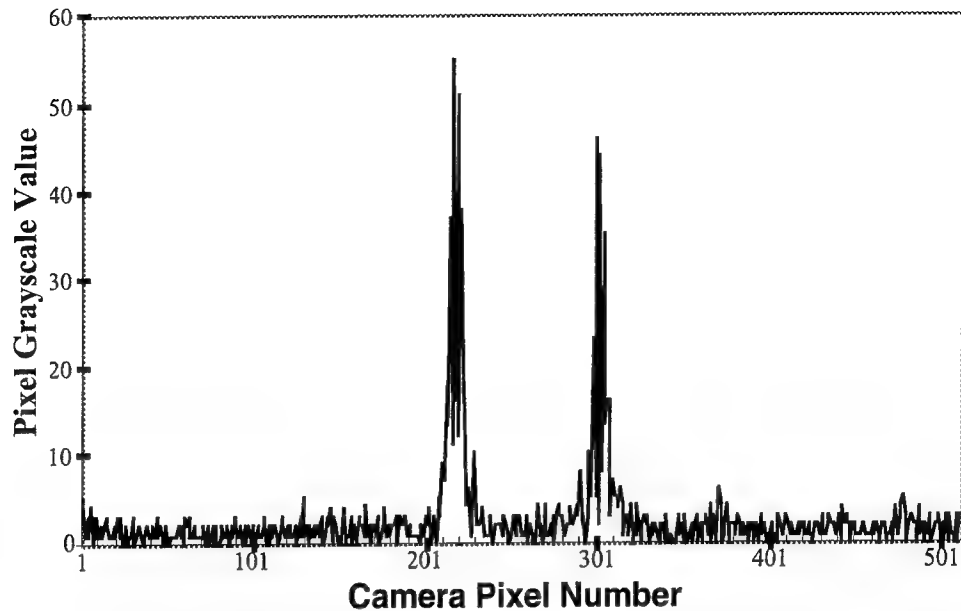


Figure 28. Normalized peak pixel location.

5.3 AO Tapped Delay Line Test Results

Figure 29 shows network analyzer traces of the magnitude response for the AOTDL. As noted, the span is 10 MHz (the design bandwidth) and the center frequency is 80 MHz. The magnitude scale is 3 dB/div. The five different plots are for different frequency inputs into the AOSLM. For example, the first figure corresponds to an input frequency of 56 MHz into the AOSLM. The remaining plots are incremented by 10 MHz in AOSLM input frequency. The bandwidth is very flat and there is not a large insertion loss variation as the tap frequencies are changed (< 9 dB variation). Figure 30 shows one magnitude response over a wider bandwidth of 25 MHz. As seen by this figure, the AOTDL has a rather large bandwidth.

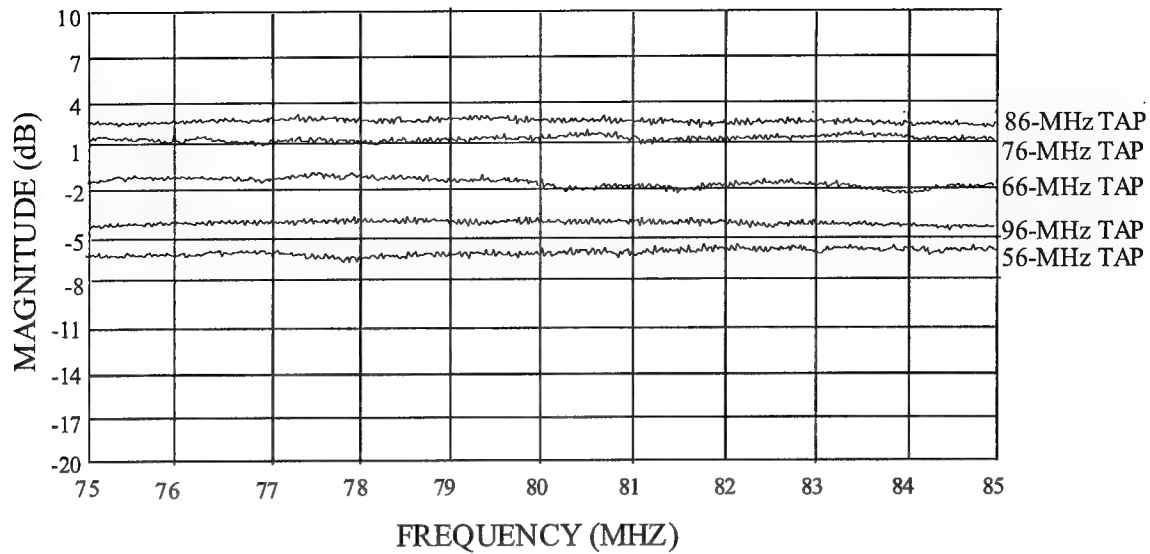


Figure 29. Various AOTDL frequency responses.

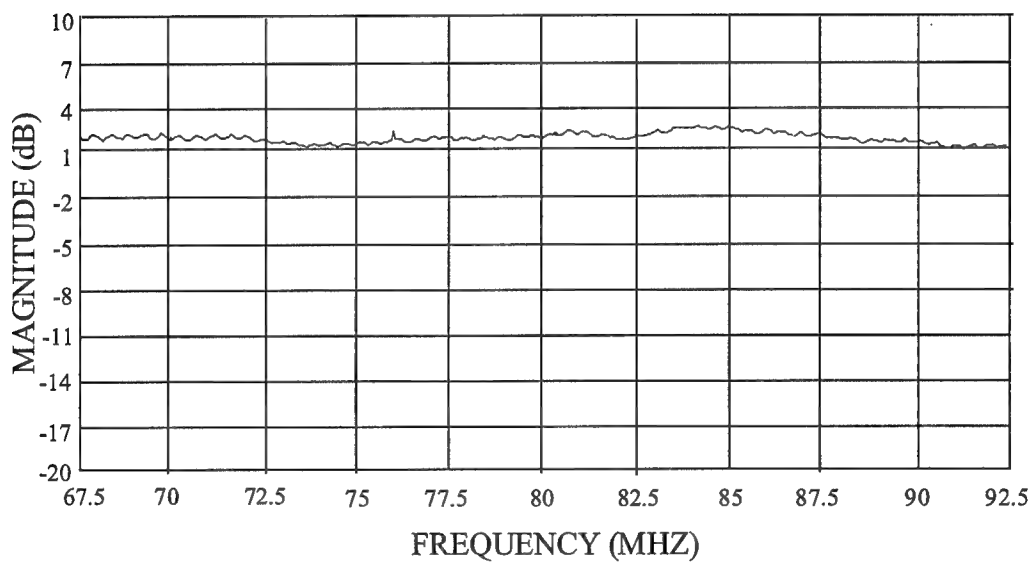


Figure 30. AOTDL frequency response for 25 MHz span.

5.4 Radar Experimental Test Results

To accommodate the 0.58 degree azimuth separation between Jammer 1 and 2 in Phase I, the radar's main receive beam was aimed as close to the desired signal while still placing the non-desired signal on the sidelobe. Figure 31 displays Phase I test results. In

the first, both the target and the jammer were tones; however, the tones were separated by 2 kHz. The spectra obtained during this test are shown in Figure 31(a). The top plot is the spectrum of the signal in the main channel of the AJOB, and the bottom plot is the spectrum of the cancelled signal out of the AJOB. In the main channel, the jammer is about 13 dB larger than the target; whereas, in the cancelled signal, the target is about 10 dB larger than the jammer. This means that the AJOB has provided a S/J improvement of about 23 dB. In the second set of Phase I test results, the jammer signal is noise and the target signal is a pulse with a width of 1 μ sec. The spectra for this case are shown in Figure 31(b). The top plot is the spectrum of the main channel signal of the AJOB, and the bottom plot is the spectrum of the cancelled signal. In the top plot, the target signal is barely discernible in the main channel signal. It is estimated that the peak of the target spectrum is 1 or 2 dB above the level of the jammer spectrum. In the cancelled signal, the peak of the target spectrum is about 15 dB above the level of the jammer spectrum. Thus, the S/J improvement for this case is about 13 dB.

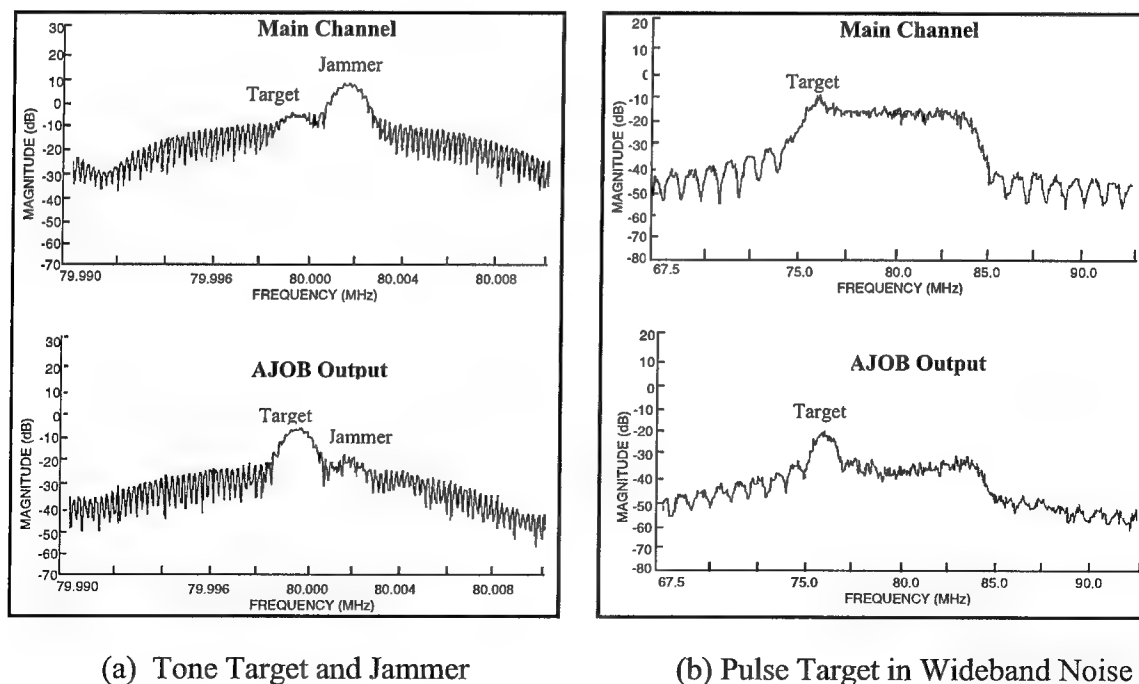
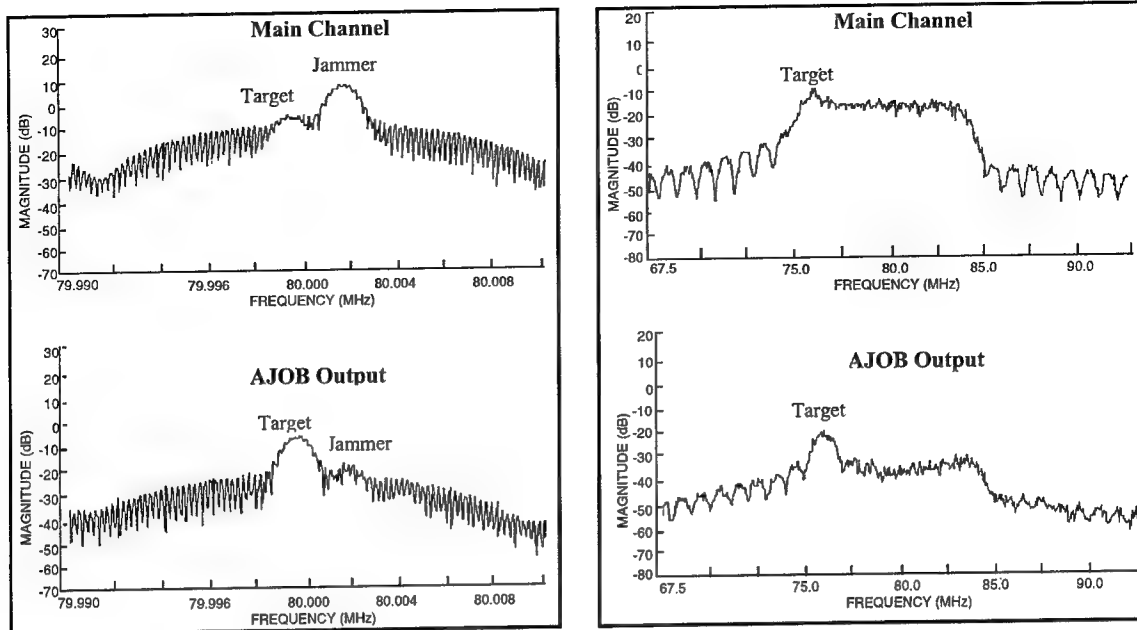


Figure 31. Phase I phased-array radar cancellation results.

Phase II achieved a much better sidelobe jamming configuration. By modifying the S-Band antenna (Figure 16), the ECCM Radar saw a 1.16 degree separation between the desired signal and the non-desired signal. This generated a better sidelobe jamming scenario, since this separation allowed the undesired signal (Jammer 1) to be placed on the receive-pattern sidelobe and the desired or target signal just in range of the main beam's 0.5 degree beamwidth. Aiming the beam closer to the target also resulted in a higher S/J ratio of 26 dB, as compared to Phase I's corresponding S/J of 14 dB.

Figure 32 displays two sets of Phase II test results. In the first test, both the target and the jammer were tones; however, the tones were separated by 1 MHz. The spectra obtained during this test are shown in Figure 32(a). The top plot is the spectrum of the signal in the main channel of the AJOB, and the bottom plot is the spectrum of the cancelled signal out of the AJOB. In the main channel, the jammer is about 8 dB larger than the target; whereas, in the cancelled signal, the target is about 16 dB larger than the jammer. This means that the AJOB has provided a S/J improvement of about 24 dB. In the second set of Phase II test results, the target signal is a tone and the jammer signal is barrage noise. The spectra for this case are shown in Figure 32(b). The top plot is the spectrum of the main channel signal of the AJOB, and the bottom plot is the spectrum of the cancelled signal. In the top plot, the target signal is 8 dB above the jammer noise floor. In the cancelled signal, the peak of the target spectrum is about 20 dB above the level of the jammer spectrum. Thus, the S/J improvement for this case is about 12 dB. This verifies the results of Phase I even though we were under full sidelobe jamming in this Phase II. Furthermore, during Phase I, the tap frequencies for the AOTDL were created manually. While in Phase II the computer, via a GPIB card, controlled the tap frequencies (i.e. the AJOB was running closed-loop).



(a) Tone Signal and Tone Jammer

(b) Tone Target in Wideband Noise

Figure 32. Phase II phased-array radar cancellation results.

6. Summary and Conclusion

Overall, the results of these two attempts to integrate the AJOB into the C-Band radar were very encouraging. The AJOB generally achieved good cancellation of the jammers and appeared to function well throughout both phases of tests. The only significant problem encountered occurred with the frequency synthesizer in the computer, which, at times, tended to generate distorted waveforms as inputs to the AOSLM in the tapped delay line subsystem. The AJOB system was able to perform closed loop, though, as can be seen in the Phase II results. The emphasis of future AJOB efforts is partitioned into three primary technical areas. In order to extend the performance capability of the AJOB and continue to demonstrate this processor within the C-Band radar testbed, the three major tasks to be accomplished include: 1) concept evaluation in realistic jammer scenarios; 2) AJOB hardware improvements; and 3) further testing of AJOB in a phased array radar.

As part of the on-going AJOB hardware improvements, there are several activities that will be pursued. They include: 1) a final decision on which time integrating correlator to use; 2) analysis of VCSEL arrays as applicable to the tapped delay line subsystem; and 3) improvements in the AJOB electronics. Having demonstrated the capability to cancel a jammer in the C-Band radar testbed, it is desirable to study the extension of this capability to multiple jammers by investigating the use of laser diode arrays to provide multiple independently addressable inputs to the tapped delay line filter. This approach provides potential for achieving faster system speed, which is currently limited by electronic interfaces. This will include the possible use of VCSEL arrays as a means of obtaining multiple, separately addressable inputs to the tapped delay line. Digital algorithms will also be developed to include carrier demodulation and filtering prior to weight calculation to improve stability of the algorithms.

REFERENCES

- [1] Friedman, D.P. Dwyer, and R.M. Iodice, "Acousto-Optic Null Steering Processor," Transition of Optical Processors into Systems 1993, David P. Casasent, Proc. SPIE 1958, pp. 83-97, (1993).
- [2] Weverka, K. Wagner, and A.W. Sarto, "Three dimensional photorefractive signal processing for radar applications," Photonic Device Engineering for Dual-Use Applications, Andrew R. Pirich, Editor, Proc. SPIE 2481, pp. 198-207, (1995).
- [3] Budge, R.J. Berinato, and M.C. Zari, "Acousto-Optic Applications for Multichannel Adaptive Optical Processor," Final Technical Report, RL-TR-92-160, (1992).
- [4] R.J. Berinato, M.C. Zari, and M.C. Budge, "Alternative Optical Architectures for Multichannel Adaptive Optical Processing," Final Technical Report, RL-TR-93-34, (1993).
- [5] Ward, C.W. Keefer, and S.T. Welstead, "Adaptive Optical Processor," In-House Report, RL-TR-91-270, (1991).
- [6] Turbyfill, M.A. Rudd, and J.L. Mack, "Active noise suppression in phased array radars using an anti-jamming optical beam-forming system," Photonic Device Engineering for Dual-Use Applications, Andrew R. Pirich, Editor, Proc. SPIE 2481, pp. 141-152, (1995).
- [7] Widrow, and S.D. Stearns, Adaptive Signal Processing, Prentice Hall, Inc., Englewood Cliff, N.J., (1985).

- [8] Sprague, and C.L. Koliopoulos, "Time Integrating Acousto-Optic Correlator," Applied Optics, Vol. 15, pp.89-92, (1976).
- [9] Abramovitz, N.J. Berg, and M.W. Casseday, "Coherent Time Integrating Processors," Acousto-Optic Signal Processing, N.J. Berg and J.N. Lee, Editors, Marcel-Dekker, Inc., New York, pp. 289-323, (1983).
- [10] VanderLugt, Optical Signal Processing, John Wiley & Sons, Inc., New York, pp. 504-530, (1992).
- [11] Zari, R.J. Berinato, M.J. Ward, and H.G. Andrews II, "Multichannel Optical Time Integrating Correlator for Adaptive Jamming Cancellation," Advances in Optical Information Processing V, Dennis R. Pape, Editor, Proc. SPIE 1704, pp. 88-97, (1992).
- [12] Ward, C.W. Keefer, and H.G. Andrews II, "Design and Fabrication of a Multichannel Adaptive Optical Processor," In-House Report, RL-TR-92-333, (1992).
- [13] Riza, "Optically Efficient Interferometric Acousto-Optic Architecture for Spectrum Analysis," Applied Optics, Vol. 31, pp. 3194-3196, (1992).
- [14] Keefer, and M.J. Ward, "Modified interferometric in-line time integrating correlator," Photonics for Processors, Neural Networks, and Memories, Joseph L. Horner, Editor, Proc. SPIE 2026, pp. 177-184, (1993).
- [15] Keefer, M.E. Turbyfill, and H.G. Andrews II, "Multichannel acousto-optic correlator for time-delay computation," Advances in Optical Information Processing VI, Dennis R. Pape, Editor, Proc. SPIE 2240, pp. 64-74, (1994).

[16]Wolfson, G.A. Uppman, "Advanced Mainbeam ECCM Technology Radar," Final Technical Report, RADC-TR-87-136, (1987).

[17]L.A. Van Brunt, Applied ECM, Vol. 1, EW Engineering Inc., Dunn Loring, VA., (1978).

***MISSION
OF
ROME LABORATORY***

Mission. The mission of Rome Laboratory is to advance the science and technologies of command, control, communications and intelligence and to transition them into systems to meet customer needs. To achieve this, Rome Lab:

- a. Conducts vigorous research, development and test programs in all applicable technologies;
- b. Transitions technology to current and future systems to improve operational capability, readiness, and supportability;
- c. Provides a full range of technical support to Air Force Materiel Command product centers and other Air Force organizations;
- d. Promotes transfer of technology to the private sector;
- e. Maintains leading edge technological expertise in the areas of surveillance, communications, command and control, intelligence, reliability science, electro-magnetic technology, photonics, signal processing, and computational science.

The thrust areas of technical competence include: Surveillance, Communications, Command and Control, Intelligence, Signal Processing, Computer Science and Technology, Electromagnetic Technology, Photonics and Reliability Sciences.